Effect of residual stress redistribution and weld reinforcement geometry on fatigue crack growth of butt welded joints

Shahani, Amir Reza; Shakeri, Iman; Rans, Calvin David

DOI
10.1016/j.ijfatigue.2020.105780

Publication date
2020

Document Version
Accepted author manuscript

Published in
International Journal of Fatigue

Effect of residual stress redistribution and weld reinforcement geometry on fatigue crack growth of butt welded joints

Amir Reza Shahani [a,*], Iman Shakeri [b], Calvin David Rans [c]

[a,*] Corresponding author. Faculty of Mechanical Engineering, Department of Applied Mechanics, K.N. Toosi University of Technology, P.O. Box 19395-1999, Tehran, Iran. Tel.: +98 21 84063221; Fax: +98 21 88677273.

E-mail address: Shahani@kntu.ac.ir

[b] PhD Student, Mechanical Engineering, K.N. Toosi University of Technology, Tehran, Iran.

E-mail address: iman.shakeri1368@gmail.com

[c] Faculty of Aerospace Engineering, Delft University of Technology, Kluyverweg 1, 2629 HS Delft, The Netherlands

E-mail address: c.d.rans@tudelft.nl

Abstract

Residual stresses and weld geometry have a significant effect on fatigue behavior of welded structures. In the present paper, redistribution of residual stress during crack growth in butt welded joint of Al5083-H111 was studied. Furthermore, the effect of post weld heat treatment and removing the weld reinforcements on fatigue crack growth rate was investigated. In order to obtain redistribution of residual stress as well as variation of residual stress intensity factor during crack growth, three dimensional simulations of welding process and fatigue crack growth were conducted for all cases. It was shown that removing the weld reinforcements causes an increase in the residual stress. It was shown that a correlation between the fatigue crack growth rate data of welded joints with base metal can be obtained by considering the weld geometry and including the redistribution of residual stresses in calculation of stress intensity factor.

Keywords: Residual stress redistribution, weld reinforcement geometry, Fatigue crack growth, Stress intensity factor, welded joint.

1. Introduction

Al-Mg alloy Al5083 has excellent corrosion resistance (even in salt water) and high toughness and so it finds wide applications in the marine, aerospace and pressure vessel industries [1]. Also, Al5083 has excellent weldability with low sensitivity to hot cracking when near-matching Al-Mg filler wire is used [2].

Most of the structures in mentioned industries are subjected to fatigue loads which lead to structural degradation and may eventually cause catastrophic failure. In addition, weld is one of the most susceptible areas in components of these structures for initiating fatigue crack. Thus, determining inspection intervals for them is very beneficial and it can be obtained by accurate data of fatigue crack growth rate (FCGR).

There are many factors intrinsic to the nature of welded joint which complicate fatigue behavior of welded components. Among them, weld geometry and residual stresses have the greatest impacts on fatigue behavior of the welded structures [3-5].

Residual stresses are come into existence as a result of plastic strains caused by local heating and cooling during the welding process. Although parts of residual stresses may be released in small-scale specimen, they play an important role on fatigue behavior of structures and should be considered in design purposes [6]. Since the residual stresses are self-balanced, they are tensile in some areas and compressive in others [7]. Depend upon the orientation of crack in weld zone, tensile or compressive residual stresses may be imposed on the crack tip and subsequently the FCGR may increase or decrease.

Ma et al. [8] proposed an experimental model for fatigue crack growth of butt welded joint considering residual stresses. The proposed model is based on the initial distribution of residual stress and redistribution of residual stress did not considered. While, it has found that the primary residual stresses are gradually released and redistributed during crack growth [9,10].

In order to completely perceive the influence of residual stresses on FCGR behavior, it is essential to consider redistribution of residual stresses caused by crack growth. Lee et al. [11] experimentally investigated redistribution of residual stress during crack growth. They considered notch as a crack and then increased the notch length by progressive saw-cuts and measured the residual stresses using the hole drilling method. The notch orientation was perpendicular to the weld line. It was observed that by increasing the notch length the longitudinal residual stress is decreased.

Miyazaki et al. [12] studied the redistribution of residual stress for a semi-elliptical surface crack using inherent strain analysis without consideration of the weld geometry. It was observed that by growing the crack through the thickness, the value of SIF changes from positive to negative.

Shiue et al. [13] studied the influence of residual stresses on the fatigue crack growth of laser-surface-annealed specimen. A dramatic change in longitudinal residual stress was noticed by introducing a notch vertical to the laser annealed zone. They also noted that the presence of tensile residual stress in front of the crack tip did not lead to increasing the FCGR of AISI 304 stainless steel. However, the effect of residual stress redistribution on SIF as well as FCGR was not analyzed in their study.

Sutton et al. [14] investigated redistribution of the longitudinal residual stress for a crack perpendicular to the weld line in Friction Stir Weld joint. The longitudinal residual stress were experimentally measured using cut-compliance technique. It was observed that by growing the crack into the weld region, the crack was arrested due to the high compressive residual stress.

Liljedahl et al. [15-17] investigated evolution of residual stresses with crack growth for MT and CT specimens using neutron diffraction method. In order to grow the crack progressively saw-cuts were conducted on samples. They observed that as the crack grows, the magnitude of residual stresses around the crack tip increases. In their works,

the crack was perpendicular to the weld line and the variation of residual SIF was not analyzed.

Servetti and Zhang [18] studied numerically the redistribution of residual stresses during crack growth vertical to the weld line. Two dimensional analysis was performed and initial residual stresses were imported to the model from experiments conducted by Liljedahl et al. [15]. It was observed that the residual SIF is always positive during crack growth. However, it was shown that the FCGR in the weld zone may not be accurately represented using two-dimensional analysis which ignores the geometry of weld profile [19].

Zhu and Jia [20] proposed a new approach to consider the effect of residual stresses on fatigue crack growth. It was assumed that the fatigue crack growth of material behaves as the diffusion of cavity and then the growing velocity of cavity was calculated. Residual stresses were measured using X-ray diffraction method. They concluded that neglecting redistribution of residual stresses will overestimate the crack growth rate and lead to a more conservative result.

In mentioned studies, the weld geometry was neglected in their analysis. While, due to the use of filler material in conjunction with backing bar in most welding processes, the weld reinforcements, which are schematically shown in Fig. 1, are formed.

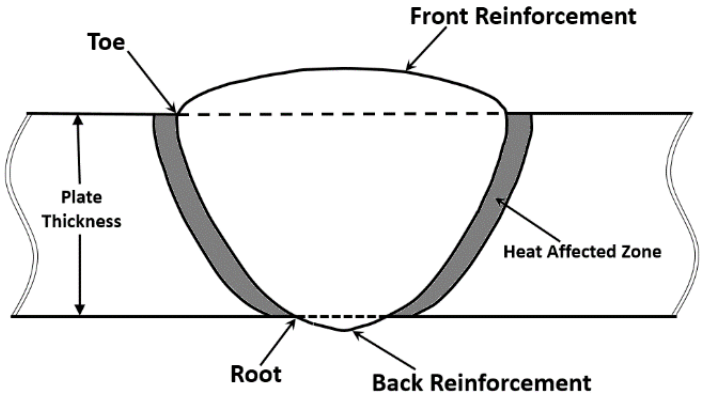

Fig. 1. The weld reinforcements in butt welded joint.

In some applications, in order to decrease stress concentration factor at weld toe and root [21], the weld reinforcements are removed. On the other hand, removing the weld

reinforcements may cause changes in the residual stresses. There is a considerable body of literature on the influences of weld geometry on fatigue behavior of welded joints from classical point of view, yet data on effects of the weld reinforcement on FCGR are scarce. Shen et al. [22] experimentally investigated behavior of fatigue crack propagation for a semi-elliptical surface crack at the weld toe in butt welded joint subjected to combined bending and compressive loads. Measuring strains experimentally, they showed that the weld reinforcements affect the nominal stress noticeably. However, redistribution of residual stresses was not considered in their work.

Employing flat plate relations for evaluating fatigue life of welded structures may result in over conservative design [19]. Nevertheless, the effectiveness of removing weld reinforcements in FCGR of welded joint is unclear, because of redistribution of residual stresses and variation of stress intensity factor (SIF) caused by the local change in weld geometry.

In the present investigation, the influence of residual stress redistribution on fatigue crack growth rate of butt welded joint of Al5083-H111 is studied. In order to justify experimental results, numerical simulations of welding process and fatigue crack growth rate are performed to obtain redistribution of residual stresses as well as variation of residual stress intensity factor during crack growth. To model the welding process, two user-defined subroutines are utilized. Also, the effect of post weld heat treatment on fatigue crack growth rate is experimentally and numerically investigated. Furthermore, the influence of removing the weld reinforcements on fatigue crack growth rate and crack front shape is examined. Since the crack grows asymmetrically, three dimensional simulation considering the bead shape is conducted to achieve the accurate value of stress intensity factor. It is observed that removing the weld reinforcements may increase the residual stresses. Considering the effect of weld geometry and including the redistribution of residual stress on the stress intensity factor, the fatigue crack growth rate results of butt welded joints can be satisfactorily correlated with results of base metal.

2. Experiments

2.1. Material specification

The material employed in this research was 5083-H111 aluminum alloy with thickness of 5 mm. The chemical composition of aluminum alloy 5083-H111 is presented in Table 1.

Table 1. Chemical composition (wt.%) of base metal and weld metal

Element	Si	Fe	Cu	Mn	Mg	Zn	Ti	Cr	Al
Base Meatal (AA5083)	0.4	0.4	0.1	0.75	4.45	0.25	0.15	0.15	bal
Weld metal (AA5183)	0.4	0.4	0.1	0.75	4.75	0.25	0.15	0.15	bal

Prior to the welding process, welding parts were wiped with ethanol in order to remove the impurities of the surfaces and a wire brush was employed to eliminate the aluminum oxide. Fig. 2 shows the Single 'V' butt joint configuration. The welding of the sheets was performed using TIG (Tungsten Inert Gas) welding process, with AA5183 used as the filler metal. The chemical composition of the filler metal is given in Table 1. The sheets were welded in a single pass and during the welding process, temporary stainless steel backing bar, as shown in Fig. 2, was used to support and shield molten weld metal. The direction of welding was parallel to the rolling direction. In order to avoid joint distortion the sheets were fixed with suitable clamps during the welding process.

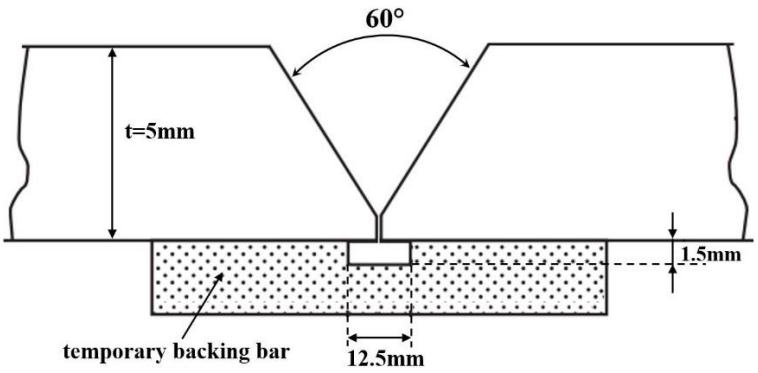

Fig 2. Joint configuration.

The welding parameters applied for TIG welding are presented in Table 2.

Table 2. Welding process parameters

Parameter	Values
Current	210 A
Voltage	10 v
Filler rod diameter	4 mm
Tungsten electrode diameter	3 mm
Welding speed	3 mm/s
Shielding gas	Argon
Gas flow rate	12 lit/min

Manufacturing tension test specimens from both base metal and welded joint, tensile experiments were performed. Table 3 shows the mechanical properties of the base metal and welded joint at ambient temperature.

Table 3. Mechanical properties of the base metal and welded joints at ambient temperature

	E (GPa)	υ	0.2% Proof Stress (MPa)	Tensile Strength (MPa)	Elongation (%)
Base metal	65±0.8	0.33	140±1.5	309±4	22.1±0.6
Welded joint	60±0.5	0.33	127±1	263±1.6	10.3±0.1

2.2. Experimental Procedure

Fatigue crack growth experiments were conducted on Compact Tension Shear (CTS) specimen, which was first introduced by Richard and Benitz [23]. Fig. 3 shows the CTS specimen geometry used in the present study. Initial notch was performed by electro-discharge machining at the center of the weld line. The direction of initial notch is parallel to the welding direction.

(a)

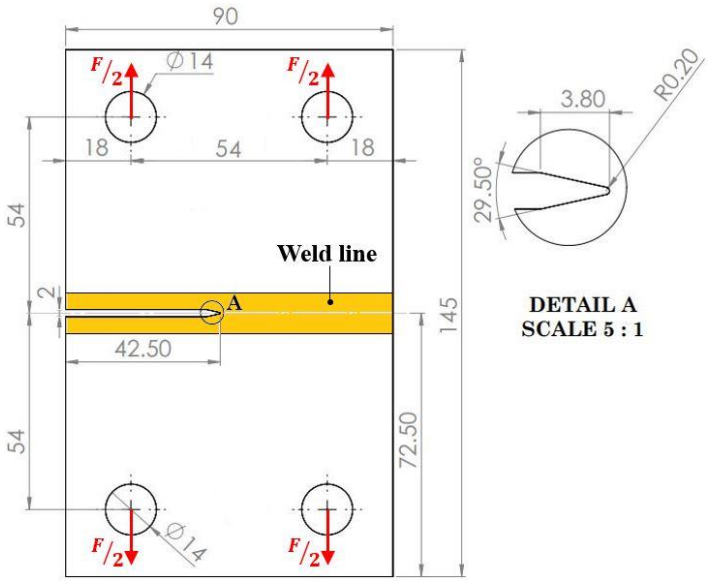

(b)

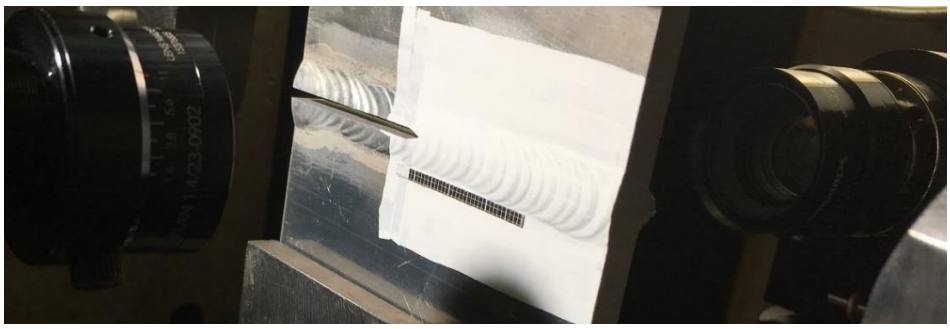

Fig. 3. (a) CTS specimen, dimensions are in mm (b) Digital cameras for measuring crack length on both sides of the specimen.

The experiments were conducted using an MTS 60 kN servo-hydraulic fatigue machine. All the tests were performed at room temperature and the loads were applied sinusoidally at a frequency of 20 Hz. During the tests, the loading ratio $R(= F_{min}/F_{max})$ was kept constant as 0.1.

Visual method has been used to measure the crack length on both sides of the specimen. For this purpose, two cameras with resolution of 2448 by 2048 consisting Point Grey processor and Linos lens have been used to record digital images of the crack tip region during crack growth. The specimen was painted ahead of the crack tip with white color for enhancing optical measurement capability of the crack length. For better distinction of the crack tip, the pictures were taken when the crack was fully open. Every 2000 cycles, fatigue loading was stopped at the minimum level and the load was increased to 95% of the maximum level and held for 1 second at this level then digital output was sent to the camera to take a picture (Fig. 4).

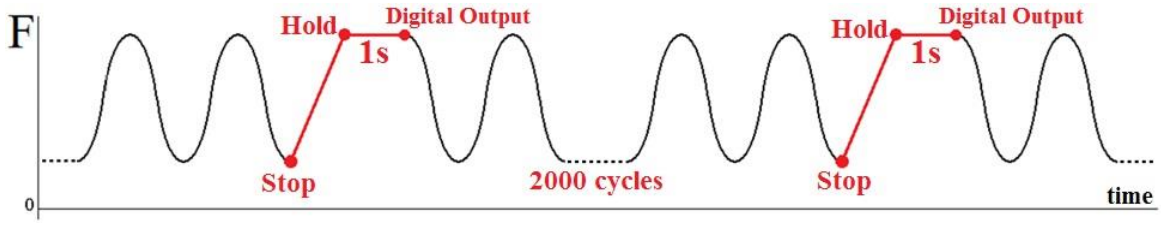

Fig. 4. Fatigue loading vs. time.

Due to the asymmetric geometry of the weld, the crack length on the two sides of the specimen varies widely. Fatigue precracking was performed under pure mode I conditions. Table 4 shows the comparison between the measured crack length during the test by digital cameras and the actual crack length at the end of the precrack stage for welded joint and base metal specimens. The actual crack length can be determined after breaking the specimen at the end of the test. The measured and actual crack length have less than 2% difference. As can be seen from Table 4, crack grows in the zigzag form in the weld metal, while in the base metal crack growth path is almost straight.

Table 4. Comparison between the measured and actual crack length for welded joint and base metal.

Crack length	Weld joint	Base Metal
Actual	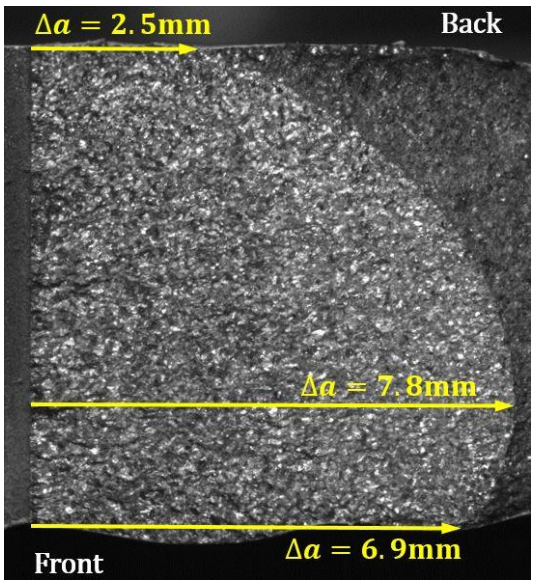	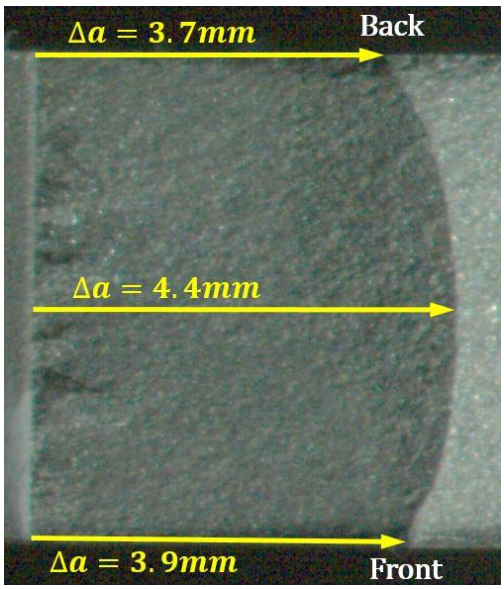

Measured		
Front	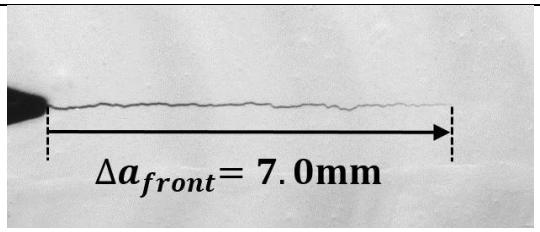	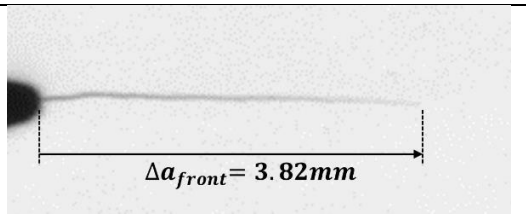
Back	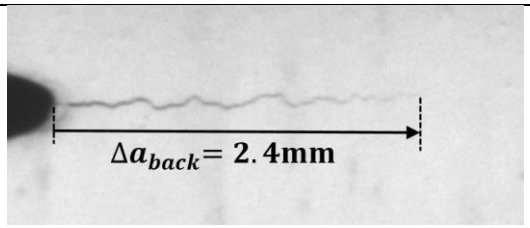	Not measured

Fatigue crack growth experiments were conducted under pure mode I conditions for base metal as well as butt welded joints. In order to investigate the effect of post weld heat treatment on fatigue crack growth and residual stresses caused by welding, a welded specimen was subjected to partial heat treatment. For this purpose, a welded specimen was kept at 250°C for 1 hour and then cooled to ambient temperature in a heat chamber. Also, in order to study the effect of reinforcement geometry on fatigue crack growth, weld reinforcements were removed from both sides of the specimen using milling machine. In order to minimize the force applied to the specimen, removing the weld reinforcements was conducted step by step and in each step less than 0.1 mm of reinforcement was removed. Then, the specimen was subjected to partial heat treatment as mentioned before. Table 5 shows the classification of specimens tested. In each case, one specimen was tested.

Table 5. Classification of specimens

Specimen code	Remarks
BM	Base metal
WM	As-welded joint
WM-HT	Welded joint with partial post weld heat treatment
WM-Flat	Weld reinforcements were removed from both side of welded joint with partial heat treatment

3. Microstructure and fracture mechanism investigations

3.1. Vickers microhardness test

The polished and etched specimen was employed for microhardness test. The Vickers microhardness across the as-welded joint was measured by a Leitz Durimet micro-hardness tester using a Vickers indenter at a load of 0.98 N. Fig. 5 illustrates the distribution of microhardness across the welded joint.

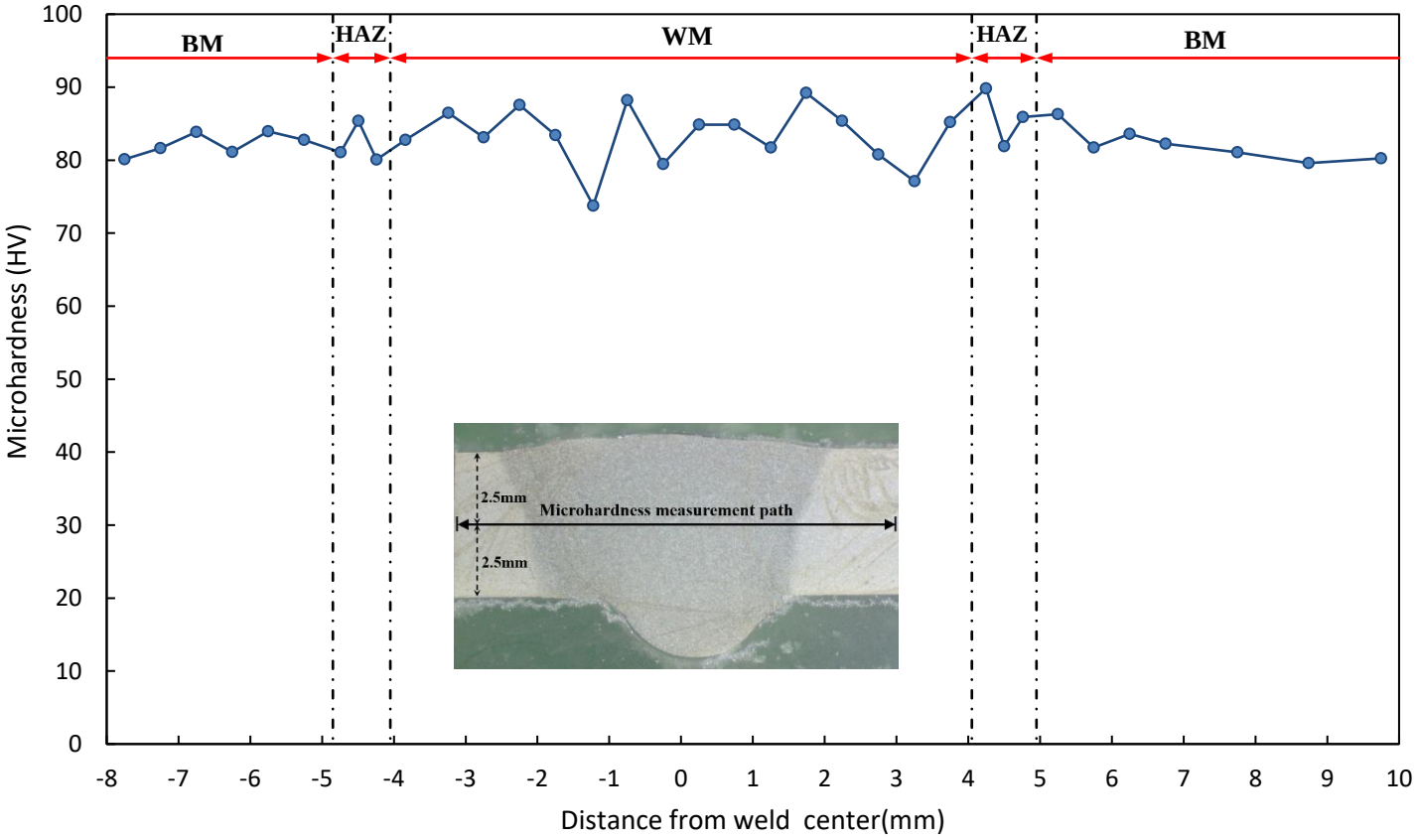

Fig. 5. Distribution of microhardness in butt welded joint

As can be seen from Fig. 5, the hardness range is almost the same in the weld metal and base metal. This could be due to their similar chemical composition (Table 1). However, the lowest values of hardness were observed at the weld zone. This reduction of hardness may probably be attributed to grains growth during the welding thermal cycle.

3.2. Microstructure examination

In order to investigate the microstructure around the weld, a specimen was extracted from as-welded joint in the transverse direction. The specimen was first polished by employing 320 to 2400 grit silicon carbide papers and diamond abrasive of 6, 3 and 1 μm on a cloth disk. During diamond polishing, propylene glycol solution was added to the rotating wheel. Then, the specimen was anodized in Barker's solution (5 mL HBF_4 (48%) in 200 mL H_2O) for 1 min [24].

Using an optical microscopy, grain structures were examined in polished and etched specimen (Fig. 6a). Also, scanning electron microscope (SEM) was used to identify grain size in different areas of the weldment (Fig. 6b).

(a)

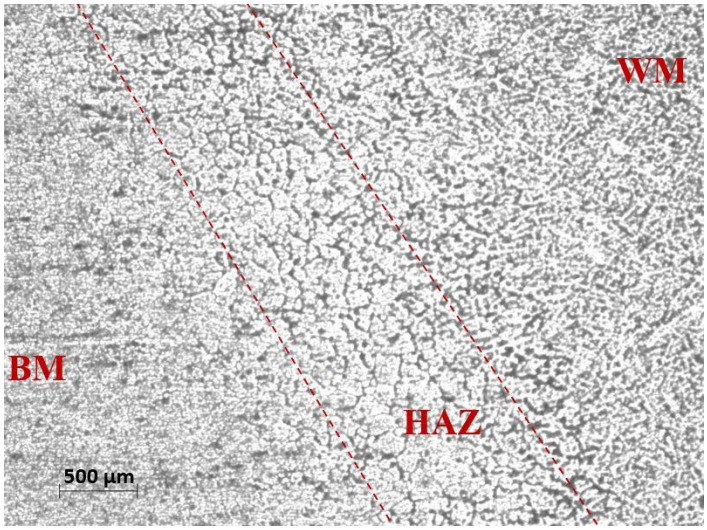

(b)

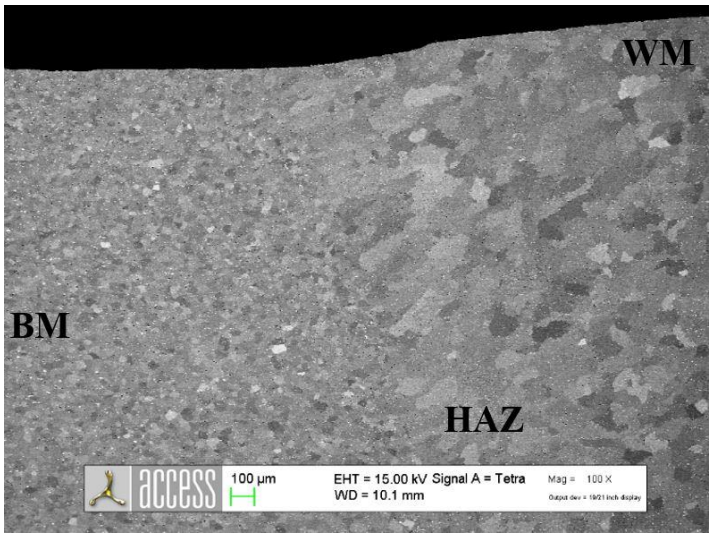

Fig. 6. Microscopic view of the different zones in the weldment through (a) optical microscope (b) SEM.

In the base metal, a typical directional microstructure is observed (Fig. 6a) which is due to the rolling process during production and this causes an increase in strength in direction of grains. On the other hand, a homogeneous non-directional equiaxed grain structure is observed in the weld zone (Fig. 6a). According to Fig. 6a and 6b, grain coarsening is observed from the base metal to the weld metal which is due to the heat diffusion into the grain. Also, it can be seen that grains in the heat affected zone are slightly larger than those in the weld metal.

3.3. Fracture surface

Fig. 7 shows the fracture surface of WM-HT specimen. It is clear that the surface of main fatigue crack is smoother than fast fracture. This occurs because the fatigue crack growth is inherently brittle, and furthermore the crack has enough time to break the molecular bonds in its initial direction. As can be seen from Fig. 7b, the main fatigue crack grows through the weld metal in the middle of the weld due to pure mode I loading conditions while, during fast fracture the crack was immediately deviated to the weld root and grew in that area.

(a)

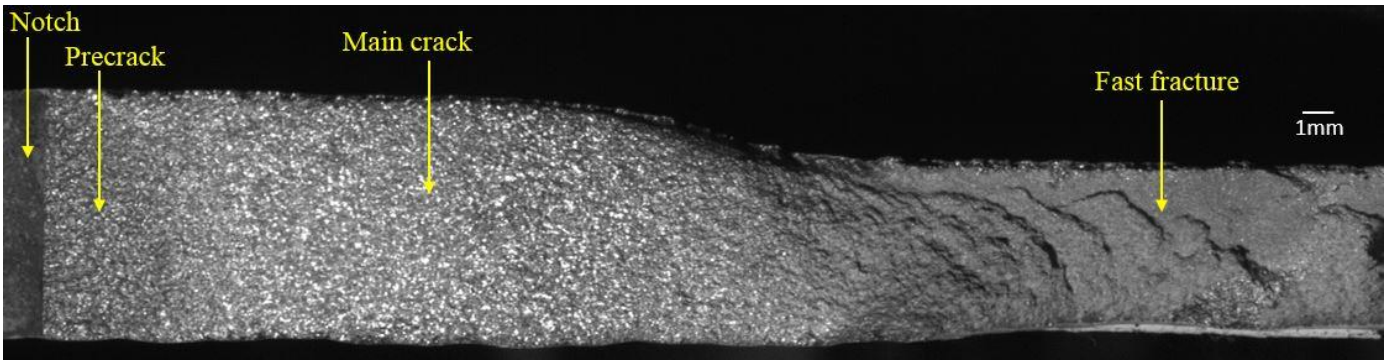

(b)

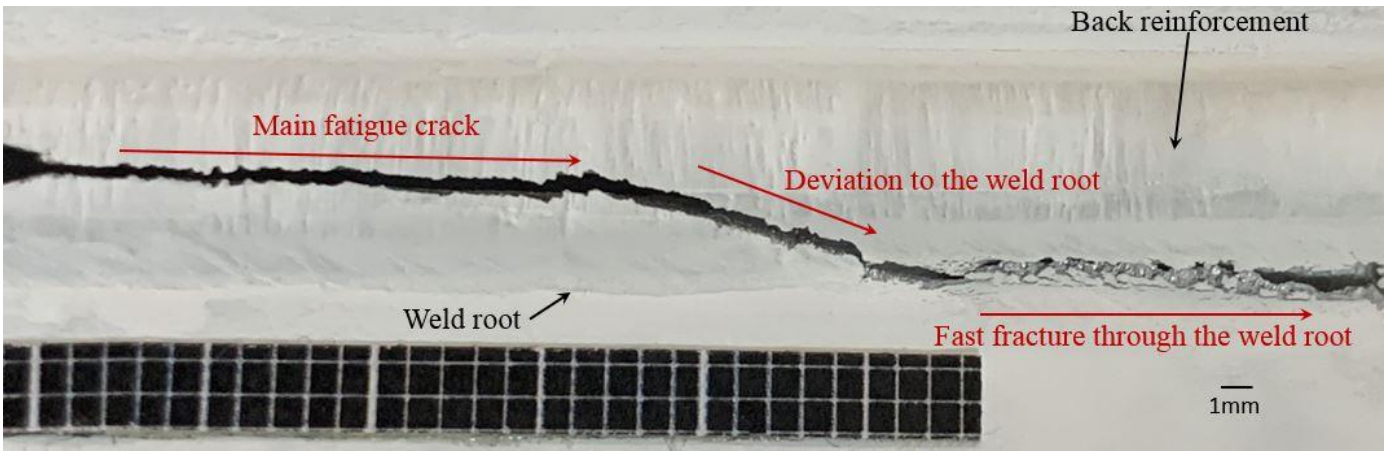

Fig. 7. Fracture surface of WM-HT specimen (a) top view (b) back view

4. Fatigue crack growth simulation

In order to obtain the precise value of the stress intensity factor (SIF) as well as the real shape of precrack, three dimensional simulation of the fatigue crack growth tests was performed using Abaqus 6.14-2 [25] and Zencrack 7.9.3 commercial software [26]. First, an un-cracked model should be created in Abaqus. The procedure of the iterative 3D fatigue crack growth prediction method is schematically shown in Fig. 8. Zencrack uses maximum energy release rate as the criterion for calculating crack growth direction. Crack growth starts with an initial size and shape of crack front. Then, the energy release rate is calculated at each node on the crack front and then, maximum value of energy release rate and crack growth direction are extracted. Afterwards, the amount of growth is determined and the crack front shape is updated. This procedure will be repeated until the crack size or the number of cycles reaches a certain limit.

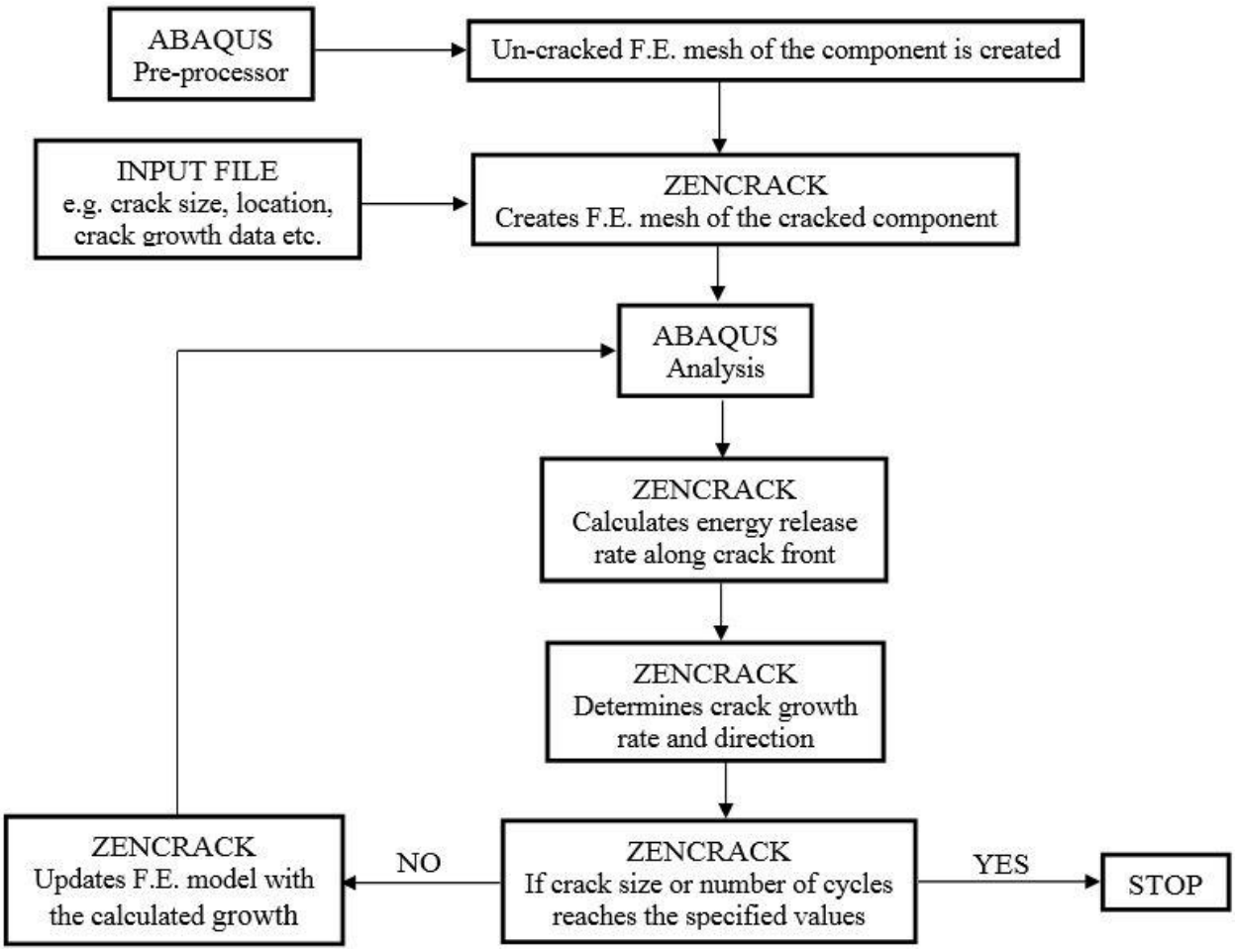

Fig. 8. Iterative procedure of 3D crack growth simulation in Zencrack.

Due to the symmetry of loading conditions as well as the geometry, half of the specimen was modeled and subsequently symmetry boundary condition was applied to the middle surface of the specimen. To apply the load, reference points (RP) were positioned at the center of the holes of the specimen and then each one was coupled to half of its respective hole. These reference points are able to distribute the applied load to the hole circumference nodes.

As illustrated in Fig. 9a,b and c, the un-cracked CTS geometries with and without weld reinforcement were created in Abaqus. Then, the regular elements at the position of crack in the un-cracked model is replaced by the crack blocks containing singular wedge elements (Fig. 9d).

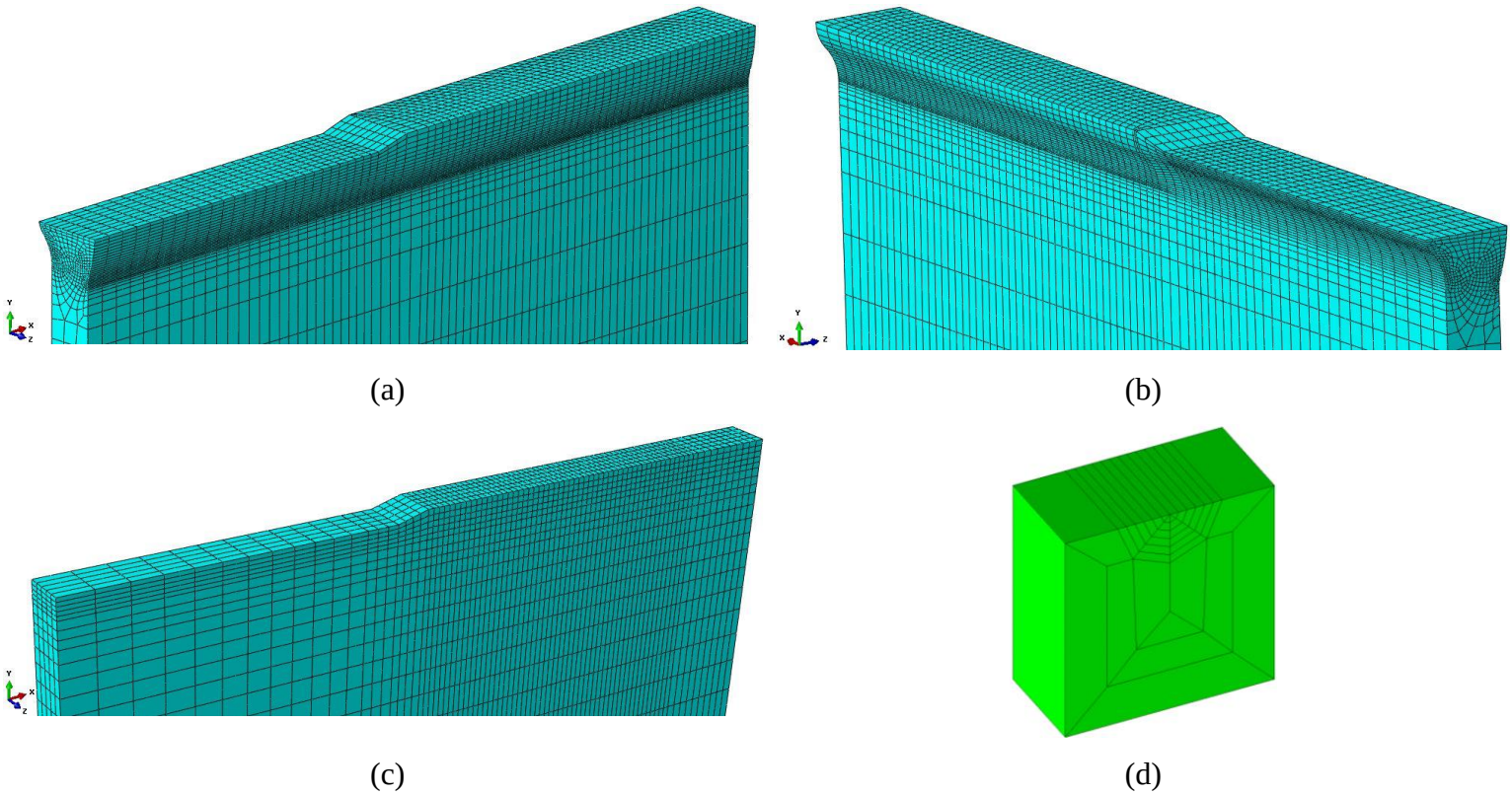

(a) (b)

(c) (d)

Fig. 9. Mesh pattern used for (a) CTS geometry with weld reinforcement, front view (b) CTS geometry with weld reinforcement, back view (c) CTS geometry without weld reinforcement (d) crack block.

The material behavior was assumed to be linear elastic. C and n of Paris relation were set to 16.5×10^{-10} and 2.03 which were obtained from curve fitting to data of BM experiment (Section 5). Hexagonal quadratic elements with reduced integration

(C3D20R) were employed for 3D finite element model. A mesh convergence study near the crack front, which is the most critical region, was performed. It was found that the elements with the size of 0.07 mm near the crack front, would provide converged SIF. Finally, the model with weld reinforcement and the flat model were discretized using 30216 elements with 133485 nodes and 16838 elements with 79397 nodes, respectively.

4.1. Stress intensity factor for CTS specimen

Richard [27] proposed the following equation to calculate the stress intensity factor (SIF) for the CTS specimen under pure mode I loading conditions in the range $0.5 \leq a/w \leq 0.7$:

$$K_{\mathrm{I}} = \frac{F\sqrt{\pi a}}{wt} . \frac{1}{1-a/w} . \sqrt{\frac{0.26+2.65\frac{a}{w-a}}{1+0.55\frac{a}{w-a}-0.08\left(\frac{a}{w-a}\right)^2}} \quad (1)$$

where F is the applied load (Fig. 3), a is the crack length (starter notch depth + fatigue crack length), w is the specimen width, t is the specimen thickness. It should be mentioned that Eq. (1) has been derived from two-dimensional models and do not consider the weld geometry and subsequently the results of SIF may not be valid for welded joint. For this purpose, 3D numerical analysis has been performed in order to obtain the actual value of the SIF considering weld geometry. K_{I} was calculated from J-integral with plane stress assumption. It is often preferred to indicate the SIF as dimensionless parameter Y_{I}, named mode I geometry factor, as

$$Y_{\mathrm{I}} = \frac{K_{\mathrm{I}}}{\frac{F\sqrt{\pi a}}{wt}} \quad (2)$$

At first, a crack with straight front was created (Fig. 10a,b). Later, the real shape of crack front was obtained by simulating crack growth. Fig. 10 illustrates the distribution of K_{I} and Y_{I} along the straight crack front obtained from the finite element analysis of the CTS specimen with $a/w = 0.5$ and $F = 4760$ N. Also, the value of K_{I}, calculated from Eq. (1), is shown in Fig. 10.

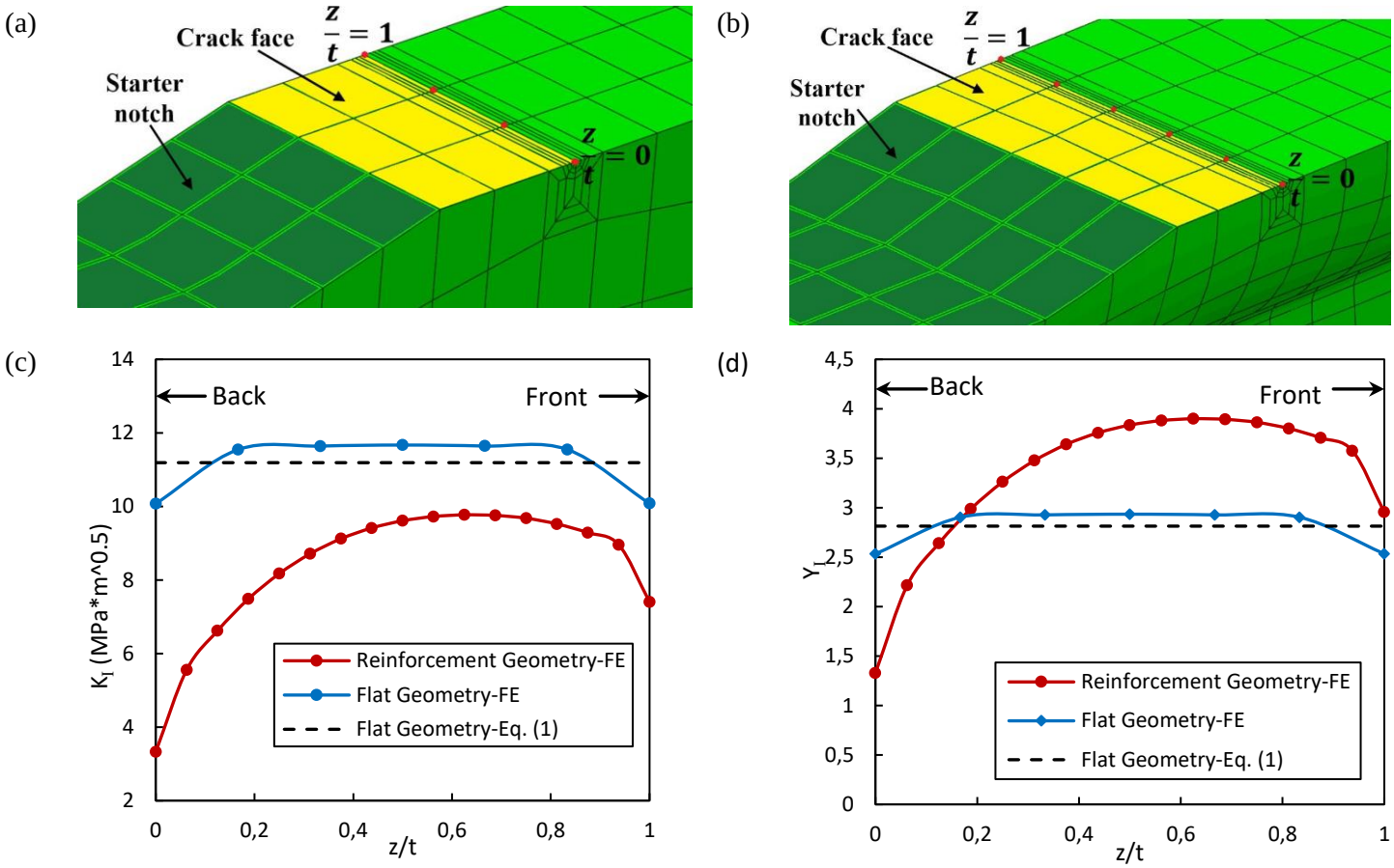

Fig. 10. Schematic view of crack face in (a) flat geometry (b) reinforcement geometry. Distribution of (c) K_I (d) Y_I, along the crack front

As can be seen from Fig. 10c, the values of K_I along the crack front for the case of considering reinforcement are less than flat geometry, since the local thickness around crack front is smaller in the flat geometry. In addition, the value of K_I in the front side of the reinforcement geometry is greater than the back side while the SIFs at both sides of the crack in flat geometry are identical. For this reason, the crack was firstly propagates from the front side of WM and WM-HT specimens. Also, it can be seen that using Eq. (1) is appropriate to estimate SIF only for flat geometry.

By simulating crack growth, the crack front is transformed from straight form to a curved shape (Fig. 11a,b). Fig. 11c,d shows the variations of mode I geometry factor (Y_I) for different nodes on the crack front during crack growth for several crack growth increments.

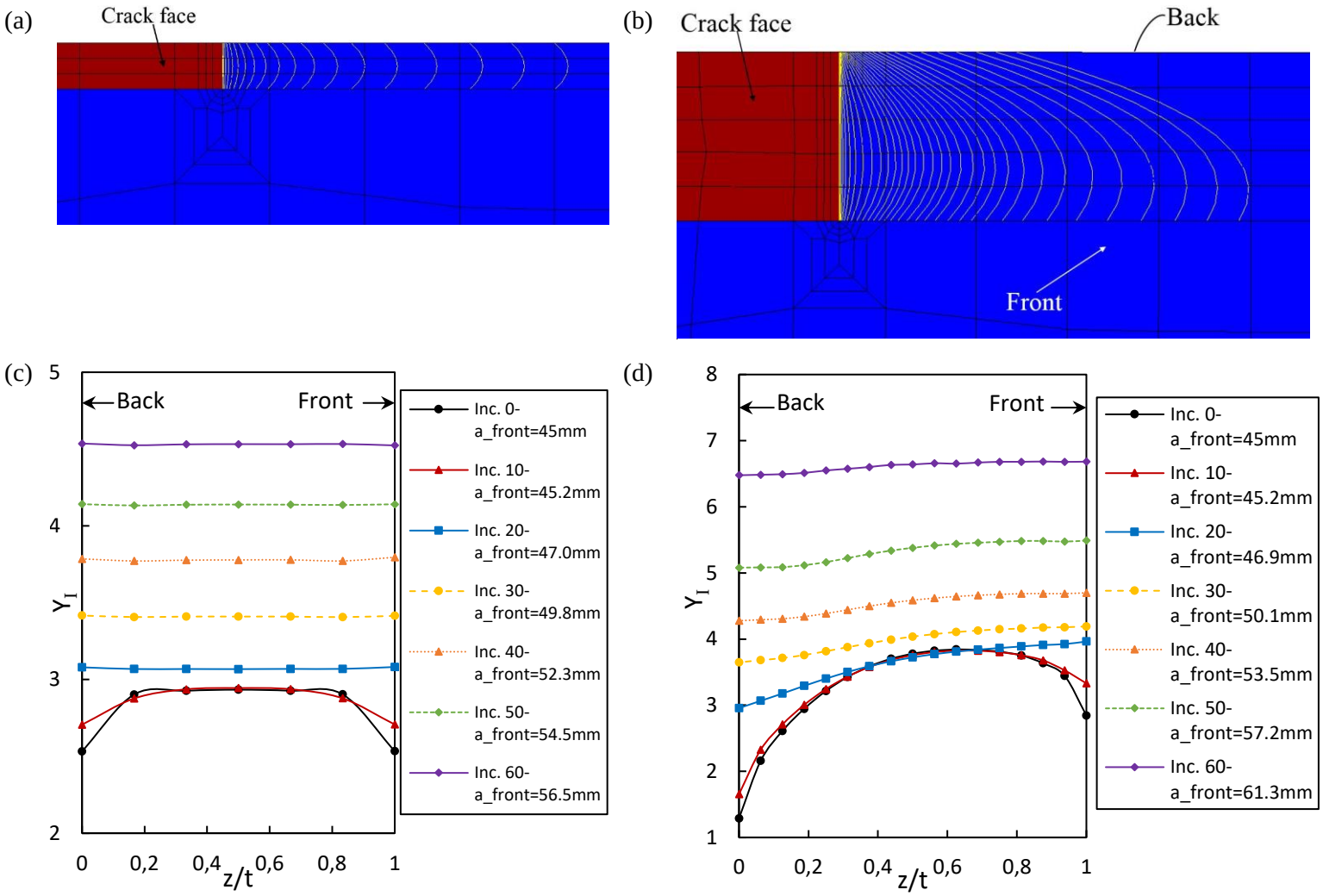

Fig. 11. Transformation of the crack front during fatigue crack growth simulation for (a) flat geometry (b) reinforcement geometry. Variations of Y_I for different nodes on crack front during crack growth for (c) flat geometry (d) reinforcement geometry.

It can be seen from Fig. 11c,d that the SIF on the crack front becomes constant with gradual crack growth. In other words, the shape of the crack front changes in such a way that the crack grows under K_I-constant conditions. The real shapes of the crack front obtained from simulation for flat and reinforcement geometry were compared with experimental results in Fig. 12.

(a)

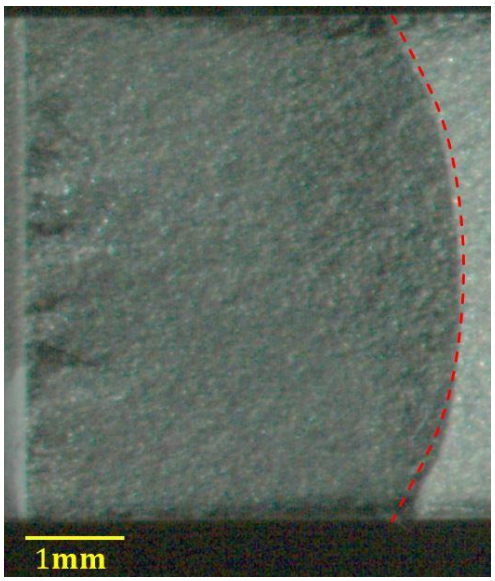

(b)

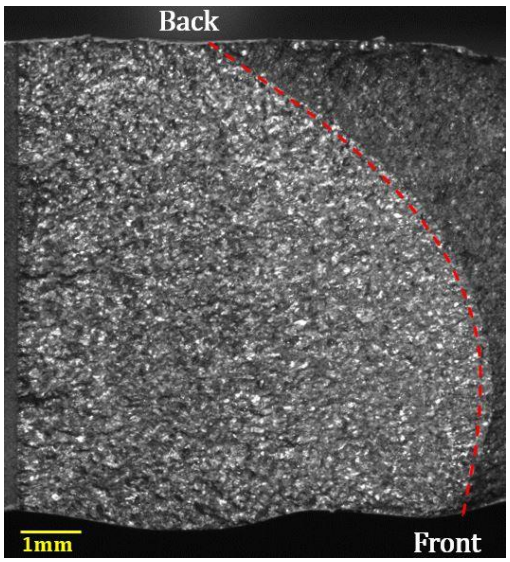

Fig. 12. Comparison of crack front obtained from simulation (dash line) and experiment for (c) BM (d) as-welded joint.

Unlike BM specimen, the crack lengths in the front and back faces of the as-welded specimen are different and so, the SIF curve in terms of crack length is different for those faces. Fatigue crack growth simulations were repeated by considering the real shape of crack front (curved crack obtained from simulation) as a precrack instead of straight precrack. Fig. 13 shows the mode I geometry factor in terms of crack length for WM and WM-Flat specimens as well as the mode I geometry factor obtained from Eq. (1) which is related to the flat specimen. It should be mentioned that the geometry factors of WM and WM-HT specimens and also BM and WM-Flat specimens are the same due to the geometrical similarity.

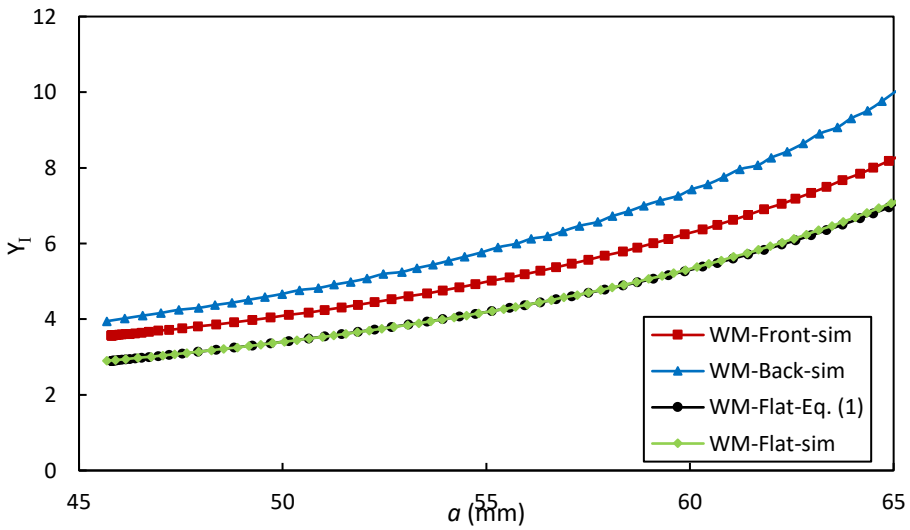

Fig. 13. The geometry factor versus crack length for different geometries

It can be seen that 27% error is appeared in calculation of geometry factor by neglecting the geometry of the weld reinforcement.

In present investigation, the applied loads for each specimen were chosen to have after fatigue precrack an actual SIF range, $\Delta K_{\mathrm{I,local}}$, of approximately 8 MPa$\sqrt{\mathrm{m}}$.

5. Experimental results

Fig. 14 shows crack length versus number of cycles for WM-HT specimen. It can be seen that the crack firstly grows in the front side of the specimen since the value of K_{I} in the front side of the reinforcement geometry is greater than the back side.

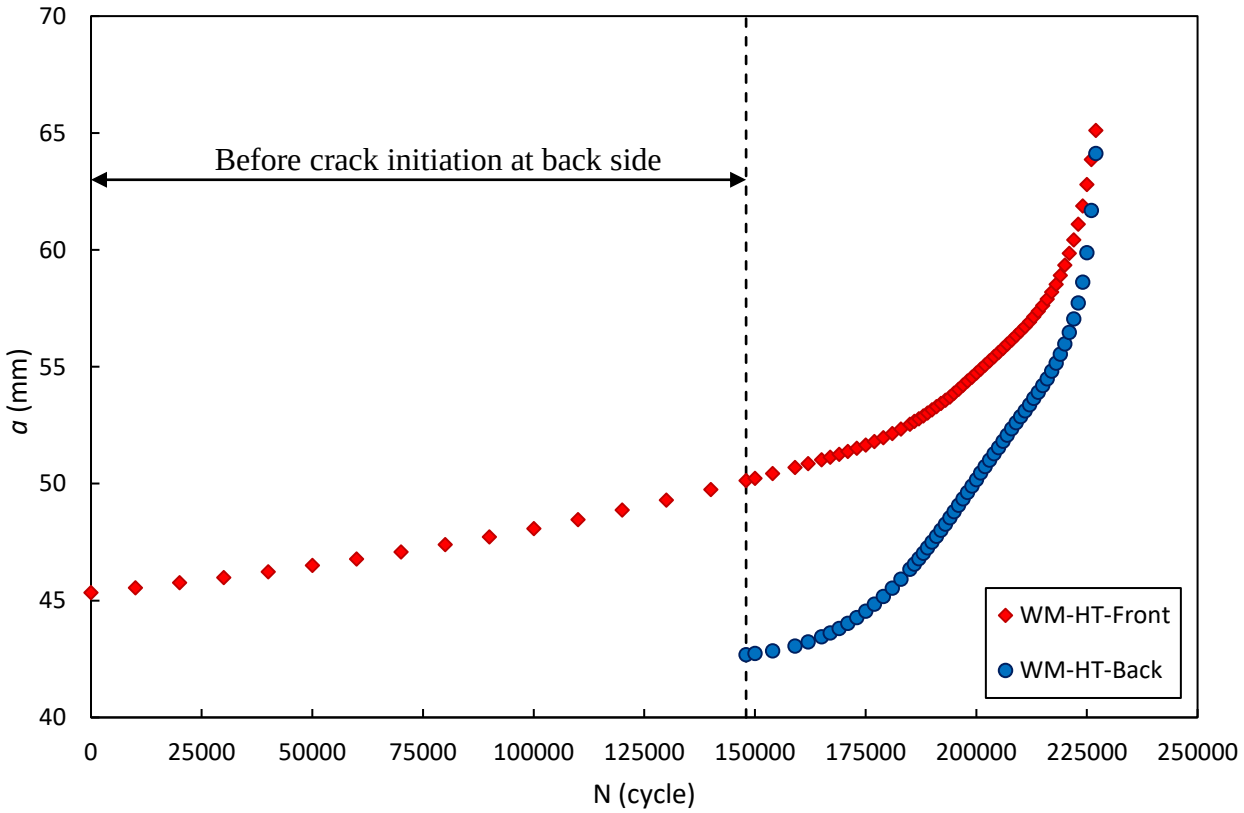

Fig. 14. Crack length versus cycle for WM-HT specimen.

Shahani et al. [28] showed that using Gaussian function instead of incremental polynomial method (proposed by standard ASTM E647 [29]) for calculating the fatigue crack growth rate, generates the similar mean values with better fitting. Therefore, the Gaussian function has been employed as data reduction method to calculate FCGRs for all the tests. This function is defined as [28].

$$a_i = a_1 e^{-\left(\frac{N_i - b_1}{c_1}\right)^2} + a_2 e^{-\left(\frac{N_i - b_2}{c_2}\right)^2} + a_3 e^{-\left(\frac{N_i - b_3}{c_3}\right)^2} + a_4 e^{-\left(\frac{N_i - b_4}{c_4}\right)^2} \quad (3)$$

Differentiating Eq. (3) with respect to N, results in:

$$\frac{da_i}{dN} = -2a_1\left(\frac{N_i - b_1}{c_1^2}\right) e^{-\left(\frac{N_i - b_1}{c_1}\right)^2} - 2a_2\left(\frac{N_i - b_2}{c_2^2}\right) e^{-\left(\frac{N_i - b_2}{c_2}\right)^2} - 2a_3\left(\frac{N_i - b_3}{c_3^2}\right) e^{-\left(\frac{N_i - b_3}{c_3}\right)^2} - 2a_4\left(\frac{N_i - b_4}{c_4^2}\right) e^{-\left(\frac{N_i - b_4}{c_4}\right)^2} \quad (4)$$

If the geometry of reinforcement is neglected, the SIF can be calculated from Eq. (1). Fig. 15a,c,e illustrates the FCGR as a function of the SIF range calculated according to Eq. (1) for all specimens. For these cases, there is no correlation between the FCGRs of front and back side of WM and WM-HT specimens. Fig. 15b,d shows the FCGRs of WM and WM-HT specimens for the state in which the FCGRs are expressed in terms of the actual SIF ($\Delta K_{\mathrm{I,local}}$) calculated in Fig. 13 which considered the geometry of reinforcement. It should be mentioned that in the case of WM-Flat specimen, ΔK_{I} obtained from Eq. (1) and $\Delta K_{\mathrm{I,local}}$ obtained from simulation are almost the same (Fig. 15e).

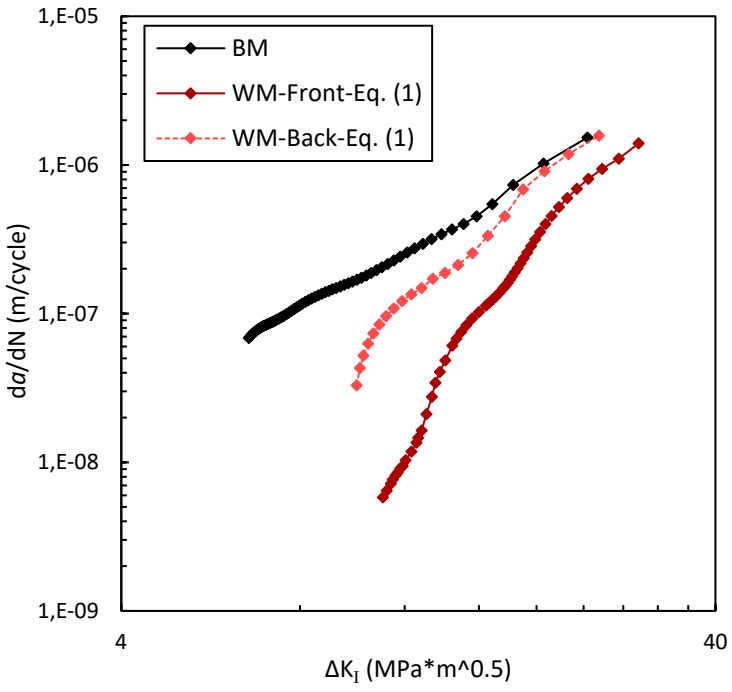

(a)

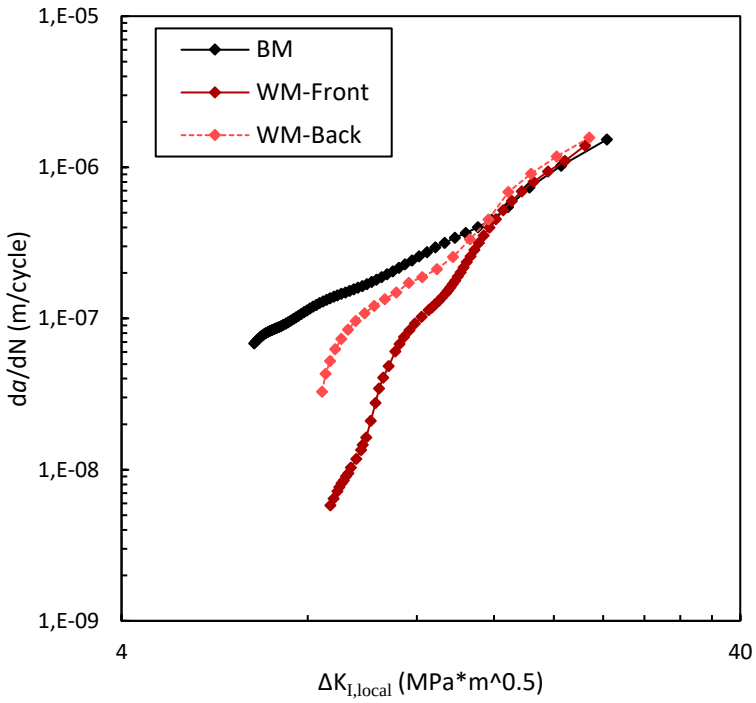

(b)

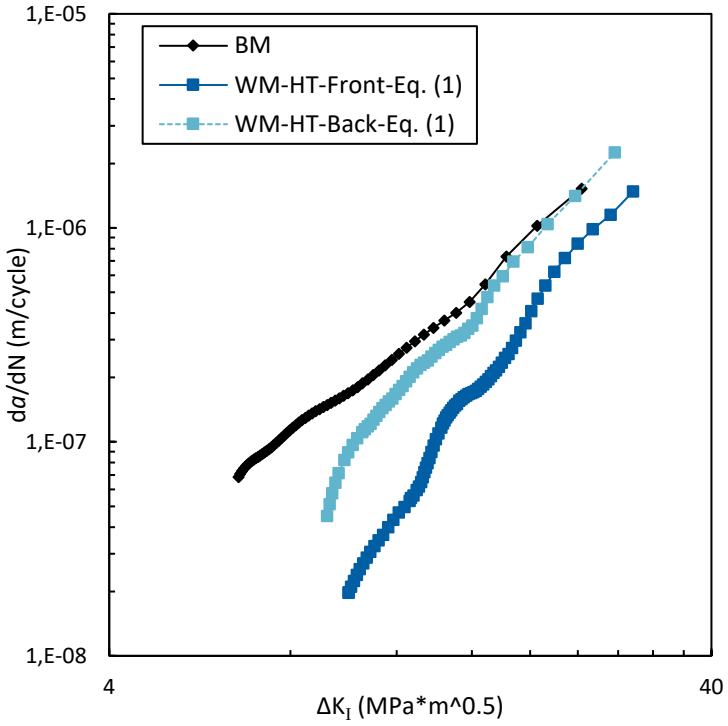

(c)

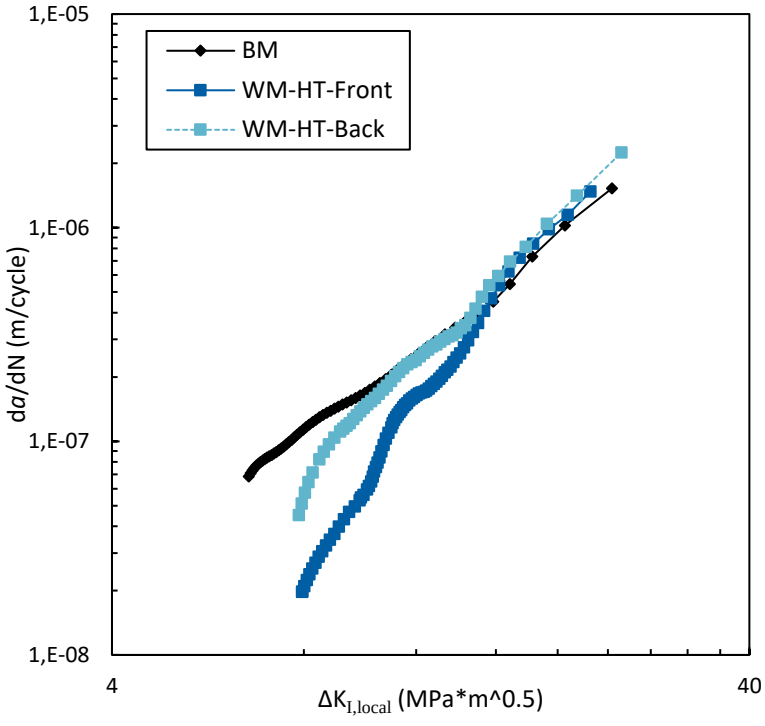

(d)

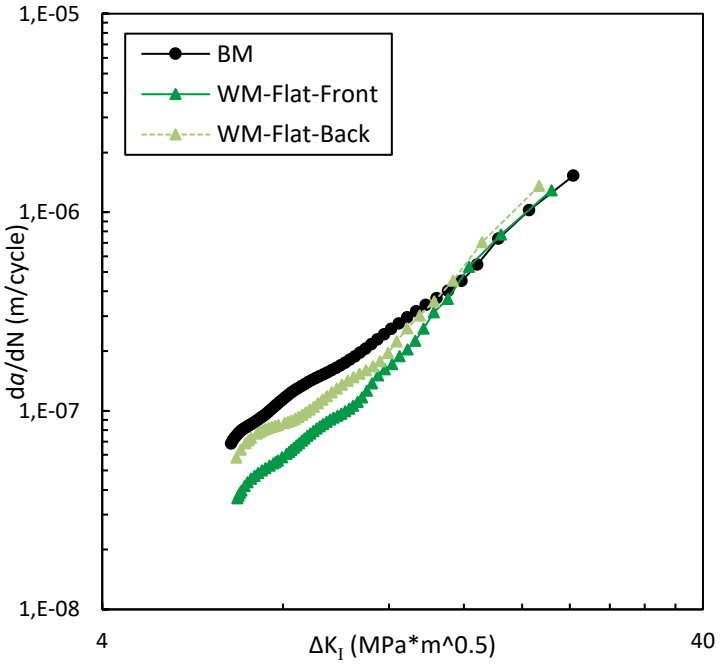

(e)

Fig. 15. Crack growth rate of WM versus (a) ΔK_{I} (b) $\Delta K_{\mathrm{I,local}}$. Crack growth rate of WM-HT versus (a) ΔK_{I} (b) $\Delta K_{\mathrm{I,local}}$. Crack growth rate of WM-Flat versus (a) ΔK_{I} (b) $\Delta K_{\mathrm{I,local}}$.

It can be clearly observed that $\Delta K_{\mathrm{I,local}}$ is able to correlate FCGRs of all welded specimens with BM satisfactorily for high $\Delta K_{\mathrm{I,local}}$ values approximately above 15 MPa$\sqrt{\mathrm{m}}$, corresponding to FCGRs in the range 4×10^{-7} to 2×10^{-6} m/cycle.

However, for $\Delta K_{\mathrm{I,local}}$ values lower than 15 MPa$\sqrt{\mathrm{m}}$ the FCGRs of welded specimens cannot be correlated further with BM specimen by $\Delta K_{\mathrm{I,local}}$ as calculated in Fig. 13. These differences appear to be due to redistribution of residual stresses during fatigue crack growth. In order to further compare the results, FCGRs for all specimens are plotted in one diagram (Fig. 16).

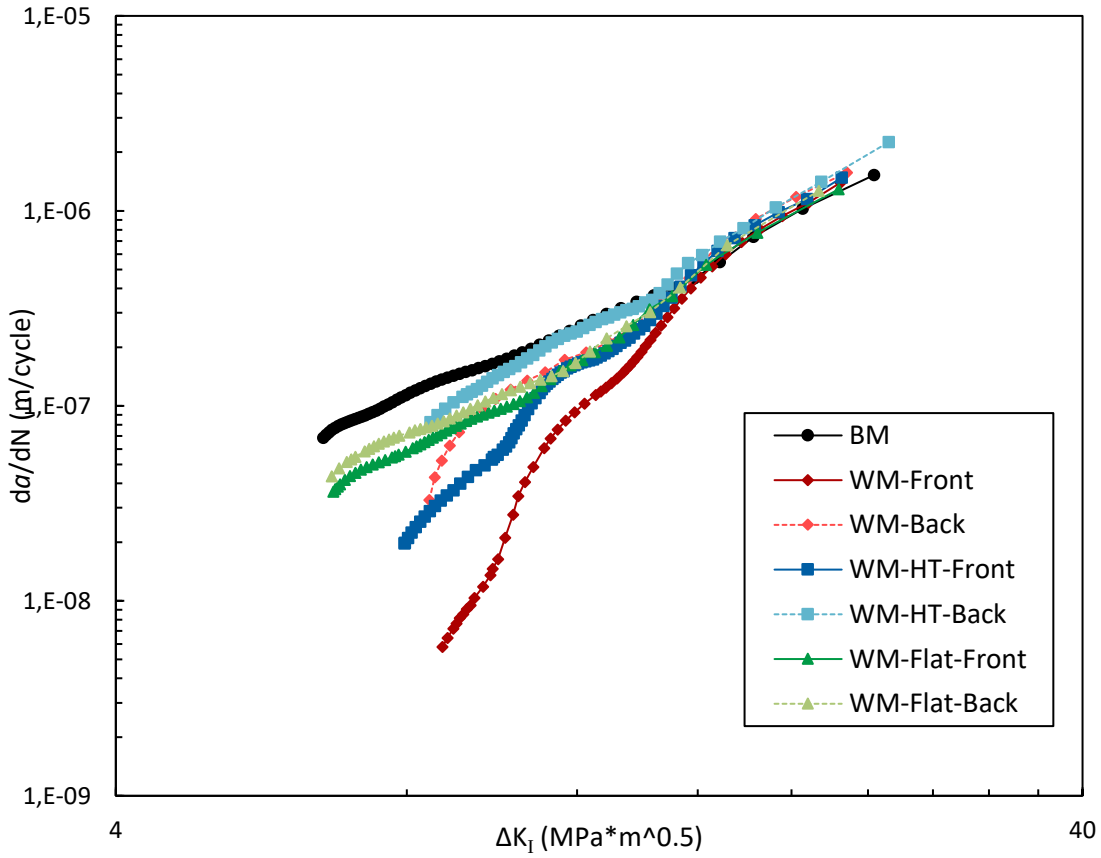

Fig. 16. Crack growth rate versus $\Delta K_{\mathrm{I,local}}$ for all specimens.

As can be seen from Fig. 16, the FCGR of WM-HT is greater than WM. This implies that there were compressive residual stresses at the crack tip and some of them have been released due to post weld heat treatment. Also, it can be seen that these residual stresses were gradually released by crack growth and after a while, the FCGRs of specimens became almost equal to each other. Furthermore, the FCGR of WM-Flat is greater than WM and WM-HT which implies that a large amount of residual stress has been released due to the removal of reinforcement and heat treatment. In addition, in all welded specimens, the FCGR at the back side is greater than the front side which

implies that the residual stresses at the back side of specimen are lower than the front side.

All the aforementioned statements are completely investigated in the next section using finite element analysis.

6. Finite element analysis

Finite element simulations were conducted to simulate the welding process of plates as well as fatigue crack growth in order to obtain distribution of residual stresses and redistribution of them during crack growth. For these purpose, two software, Abaqus 6.14-2 [25] and Zencrack [26], were employed. Fig. 17 shows the various steps of FE simulations.

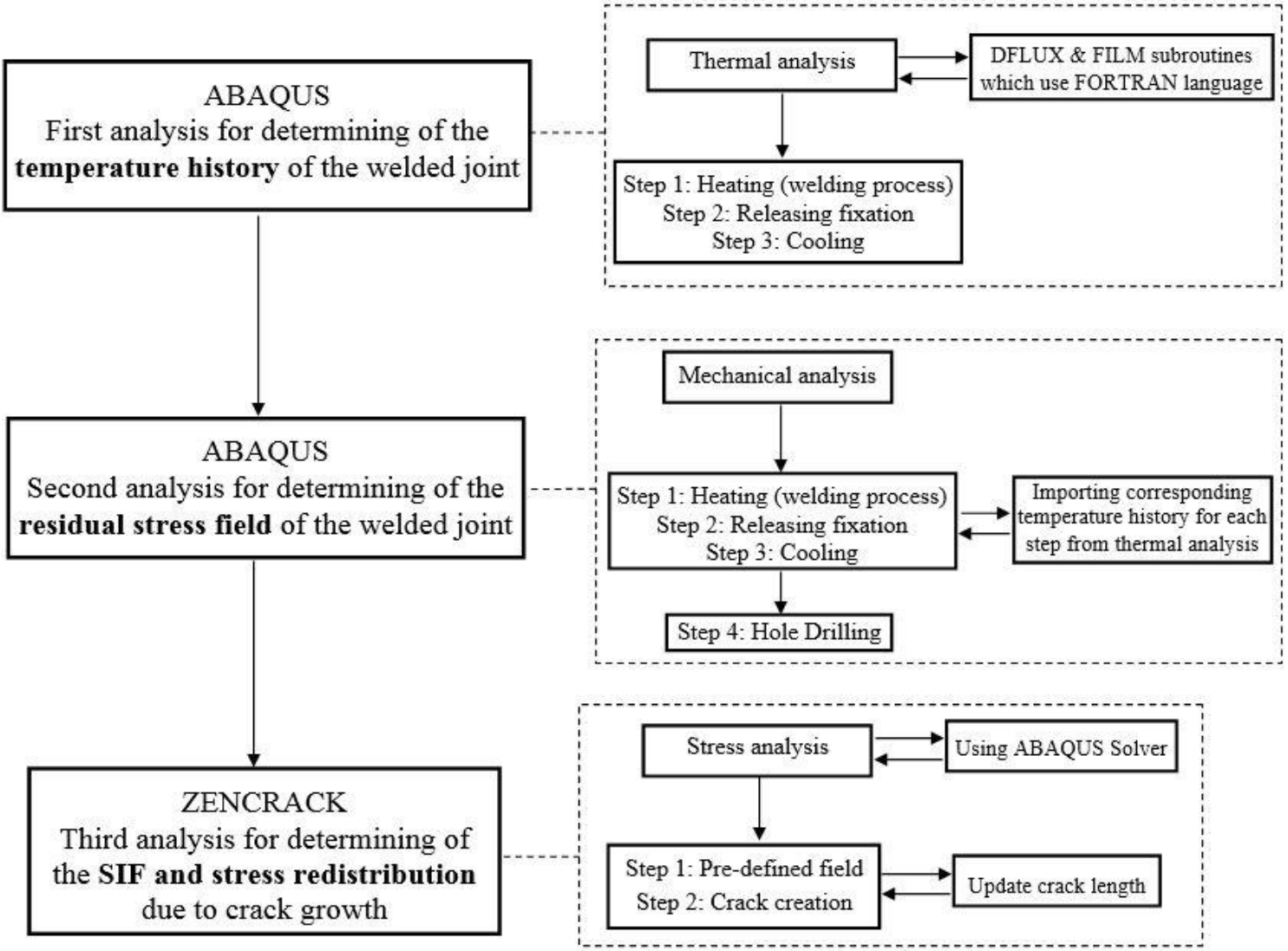

Fig. 17. Steps of finite element simulations

6.1. Welding simulation

3D finite element simulation of the welding process was conducted using Abaqus. The sequentially coupled thermomechanical analysis was accomplished, in which heat transfer analysis was followed by mechanical analysis. It means, a thermal analysis was firstly performed to achieve the temperature history of the plate. Thereafter, the temperature history was incrementally applied to the mechanical analysis in order to determine the residual stresses. That is, in mechanical analysis the temperatures of nodes were read from an output file which produced during thermal analysis.

Due to the symmetry of loading conditions as well as the geometry, half of the specimen was modeled (Fig. 18). Hexagonal quadratic heat transfer elements (DC3D20) were employed for the thermal analyses. The size of the meshes employed in the mechanical and thermal models was identical. In the mechanical analyses, hexagonal quadratic elements with reduced integration (C3D20R) were used. A mesh convergence study on the weld centerline was performed by changing the size of elements. It was found that the elements with the size of 0.2 mm near the welding zone, would provide converged temperatures as well as residual stresses. Eventually, the model was discretized using 62550 elements and 278741 nodes.

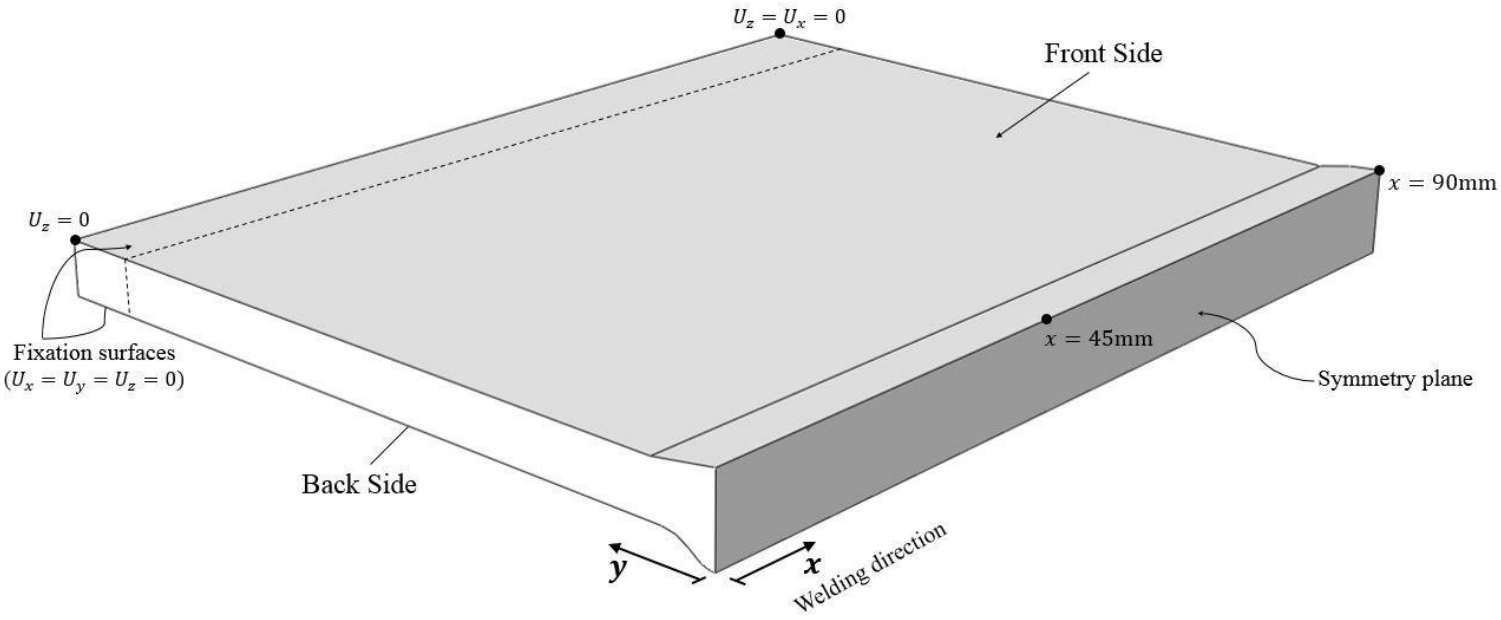

Fig. 18. Schematic view of half of the specimen modeled

6.1.1. Material properties

Fig. 19 and Table 6 show the material properties employed in the FE analysis. Tensile tests were carried out under various temperatures to obtain variation of mechanical properties in terms of temperature (Fig. 19b). The temperature of specimens was directly measured using thermocouple. The material softening at elevated temperatures can be considered by the reduction in the Young's modulus at high temperatures. At high temperatures equal to the melting temperature, the value of Young's modulus nearly approaches zero and subsequently divergence problems occur due to numerical instabilities. In order to solve mentioned problem, the value of Young's modulus at melting point was considered as 0.00007 GPa. Since physical properties of 5xxx series aluminum alloy do not vary in the wide range, the values for Al5083-H116 [30] were used (Fig. 19a).

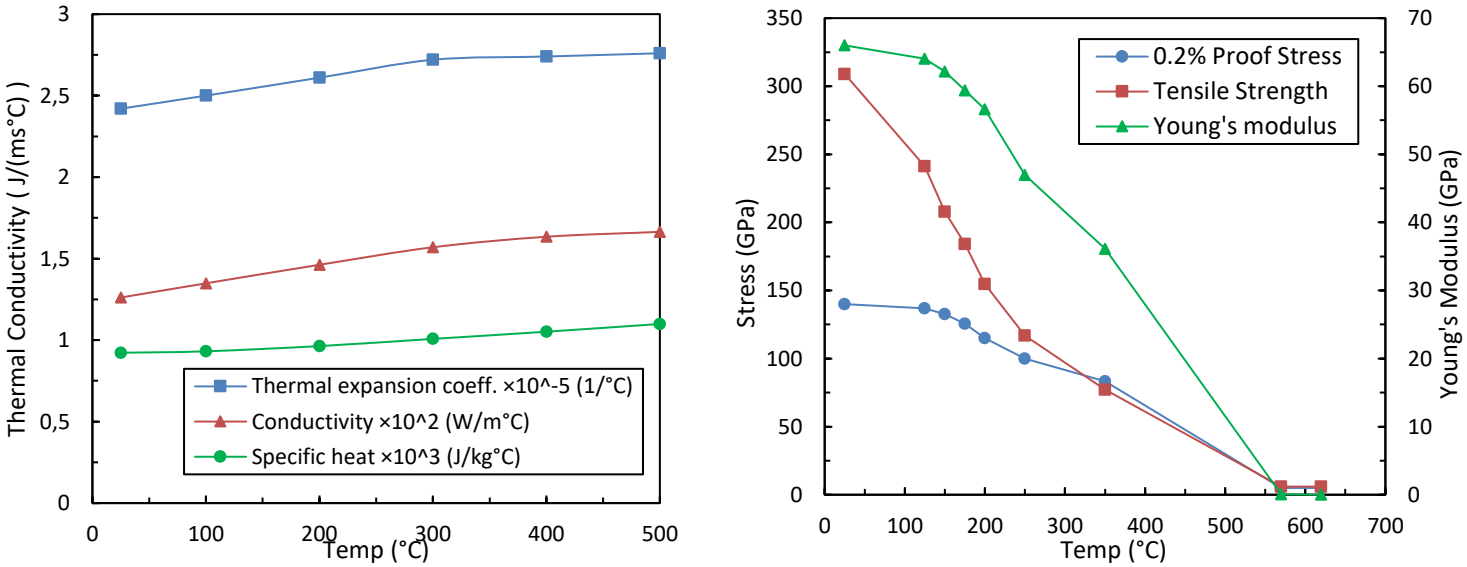

(a) (b)

Fig. 19. (a) The physical and thermal properties of Al5083-H116 [30] (b) The mechanical properties of Al5083-H111 obtained from present investigation

Table 6. Material properties of aluminum alloy [31]

Density (kg/m^3)	2640
Latent heat (J/kg)	300000
Melting range $(°C)$	570-620
Poisson's ratio	0.33

6.1.2. Thermal analysis

The welding process parameters presented in Table 2 were employed in the thermal analysis of welding. As mentioned before, half of the specimen was modeled due to the symmetry (Fig. 18). A moving distributed heat flux was applied as a heat source on the front surface of the plate. According to the Friedman model [32], it was assumed that the heat source with a circular shape is perpendicularly applied to the surface. The heat flux should be calculated at a certain time and location on the surface of elements on which the heat flux is acted. For this purpose, a user subroutine named DFLUX, which uses the FORTRAN language was developed and included in the model. The distribution of heat flux is stated as Eq. (5) [32]:

$$q(r) = \frac{3Q}{\pi r_b^2} e^{-3(r/r_b)^2} \tag{5}$$

where Q is the heat input and for arc welding it can be calculated as following equation [33]:

$$Q = \eta VI \tag{6}$$

where I and V are the arc current and voltage, respectively. η is the arc efficiency and was assumed to be 90% for the TIG welding process [33]. r, as illustrated in Fig. 20, is the distance between the point in which the heat flux is calculated and the center point of the heat source and it is expressed as:

$$r = \sqrt{(x - x_h)^2 + y^2} \tag{7}$$

where x_h is the location of center point of moving heat source and it can be determined at each moment as Eq. (8):

$$x_h = vt \tag{8}$$

where v is the welding speed. It can be seen that by increasing the time (t) the heat source area is moved on the front surface of the plate. It was determined in the subroutine that if the value of r is equal to or less than r_b, Eq. (5) is used to calculate

the heat flux. If not, the heat flux is set to zero. r_b characterizes the heat input distribution and specifies the area in which 95% of the heat flux is deposited and it was set to 5.5 mm based on the weld pool size [31].

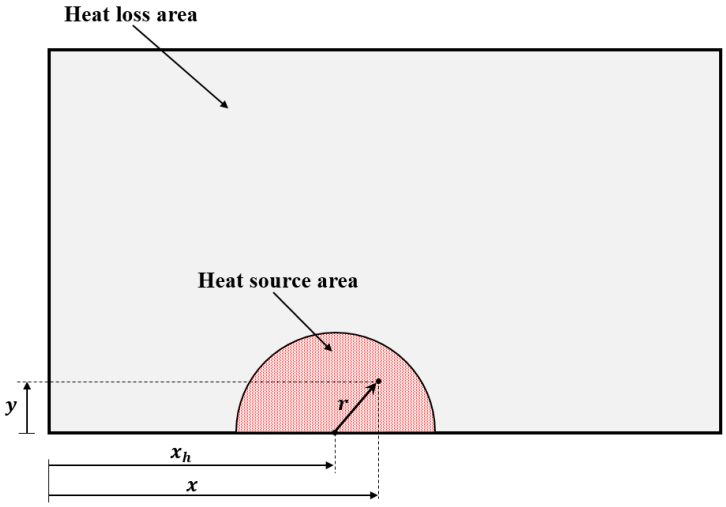

Fig. 20. Region of the heat source and het loss.

The convection and radiation to the environment were considered as the thermal boundary conditions for all faces of the specimen except the symmetry plane (Fig. 18) and the region on which the heat source is acted. The heat loss can be evaluated by Eq. (9):

$$q = q_{\text{convection}} + q_{\text{radiation}} = h_{\text{convection}}(T_i - T_a) + \varepsilon_{\text{em}}\sigma_{\text{bol}}(T_i^4 - T_a^4) \quad (9)$$

where T_a and T_i are the ambient temperature and expected temperature of the current increment, respectively. $h_{\text{convection}}$ is the convection coefficient and it was set to 8 $W/m^2\,°C$. It was presumed that $h_{\text{convection}}$ is constant since it depends primarily upon the environment temperature [33]. The emissivity, ε_{em}, is 0.15 for aluminum and the Stefan-Boltzman constant, σ_{bol}, is 5.67037×10^{-8} $W/m^2\,°C^4$ [34]. Also, the ambient temperature was set to 20°C.

As the heat loss area changes over the time for the front face of specimen, another subroutine, named FILM, was developed and employed with DFLUX. In the developed code, if the location under consideration is located within the circular area where the flux is acted, no heat loss occurs. Otherwise, the heat loss coefficient, which consists of both the radiation and convection coefficients, is calculated as follows:

$$h_{\text{total}} = h_{\text{convection}} + \varepsilon_{\text{em}}\sigma_{\text{bol}}\left(T_i^3 + T_i^2 T_a + T_i T_a^2 + T_a^3\right) \quad (10)$$

therefore, the total heat loss is calculated as:

$$q = h_{\text{total}}(T_i - T_a) \quad (11)$$

After the heat source reached the end of the specimen, the fixation of nodes under the clamp was released during 1s. Thereafter, the specimen was cooled down until the steady state during 2000s.

6.1.3. Results of the thermal analysis

Fig. 21 shows the distribution of temperature in the specimen during motion of the heat source in thermal analysis at various times. It can be seen that the maximum temperature occurs on the front surface and at the center of the heat source.

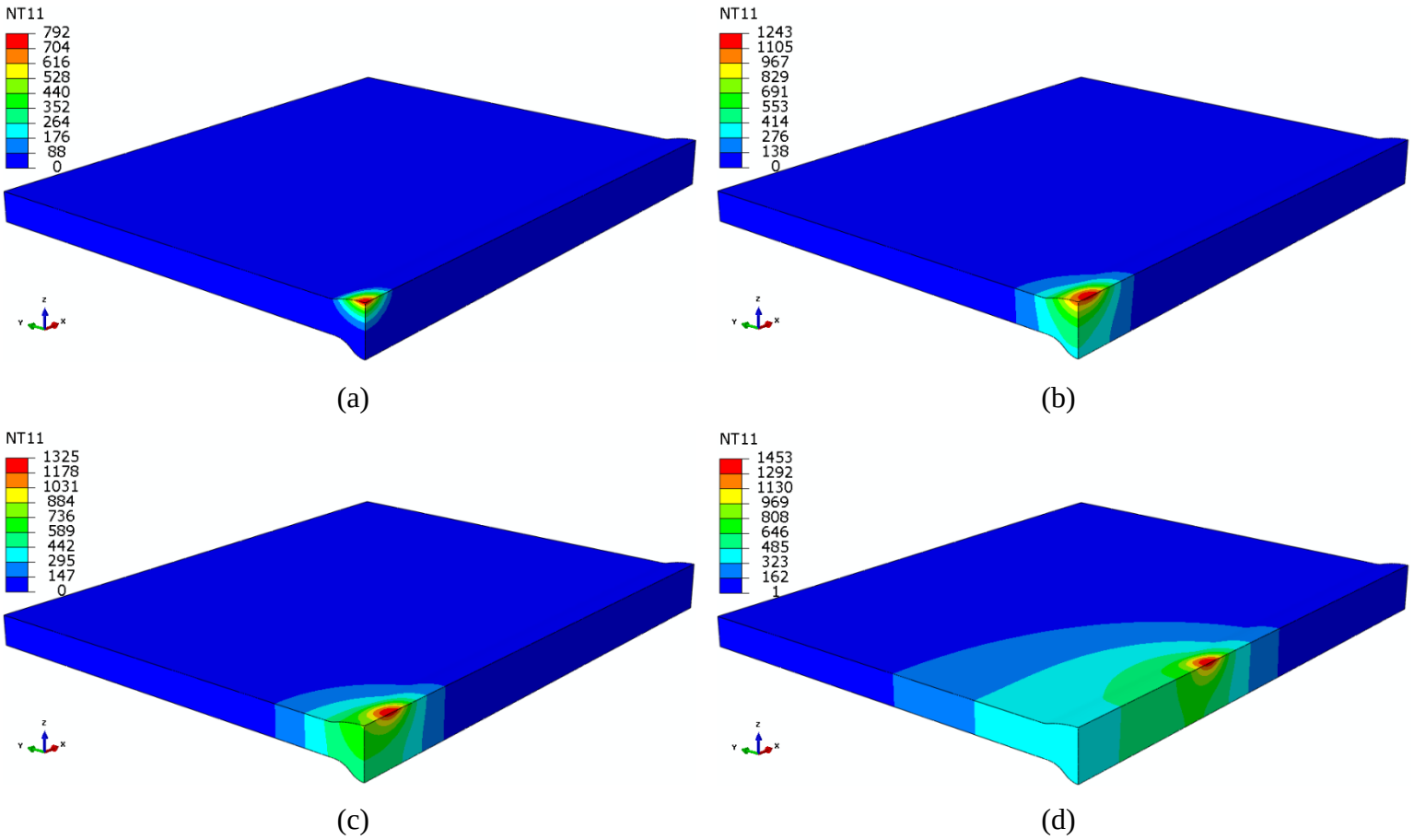

Fig. 21. Distribution of temperature during motion of the heat source in thermal analysis at (a) t=0.1s (b) t=1s (c) t=2s (d) t=10s

Fig. 22 illustrates the temperature history at different locations of the specimen.

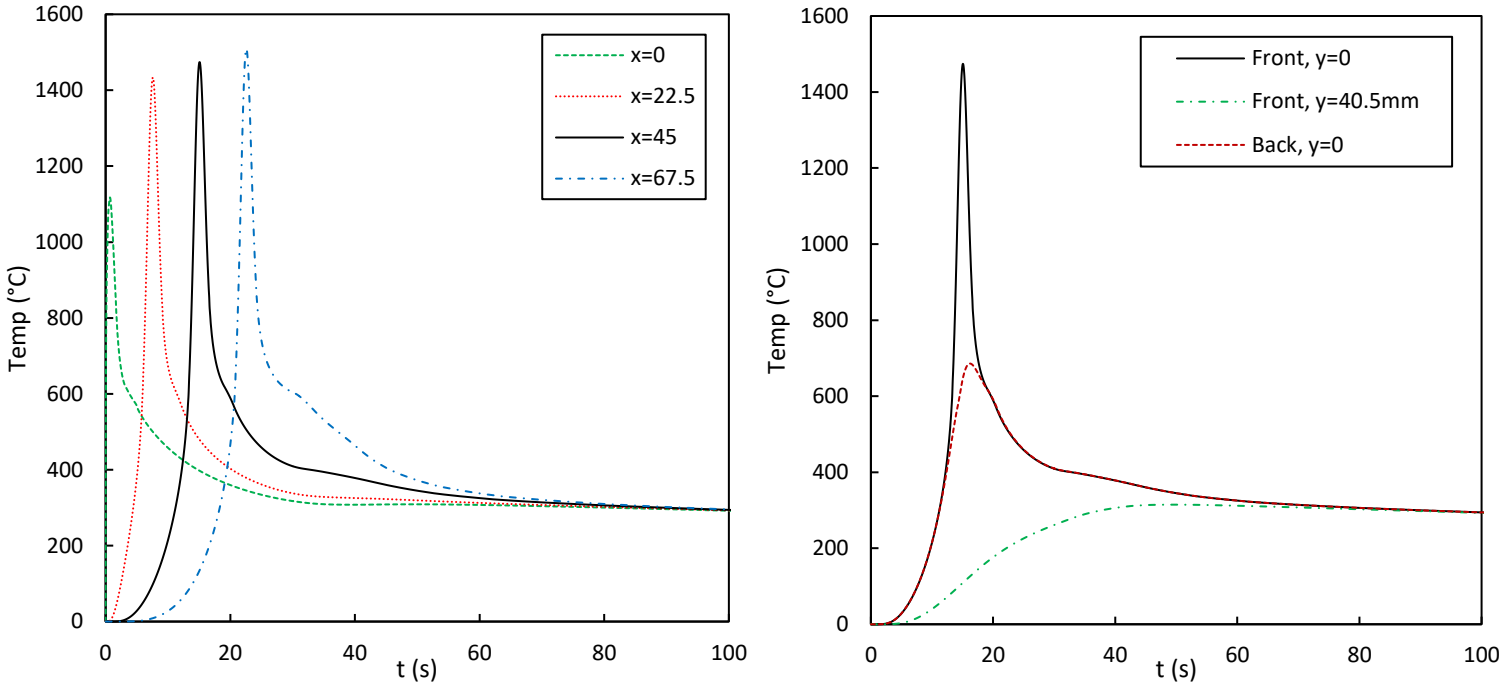

(a) (b)

Fig. 22. Temperature history at (a) the weld centerline, y=0 (b) middle section, x=45mm.

As can be seen from Fig. 22a, the maximum temperature at nodes where the heat source reaches them later, increases further due to preheating caused by the heat source. Moving away from the weld centerline, the temperature decreases (Figs. 21, 22b).

6.1.4. Verification of thermal model

In order to verify the developed subroutines in thermal model, the problem which was performed by Fanous et al. [], was modeled. A plate with width of 50 mm (y direction), length of 100 mm (x direction), and thickness of 2.5 mm was considered. The welding speed, arc voltage, arc current and arc efficiency were 2 mm/s, 24 V, 30 A and 90%, respectively. The material used was Inconel Alloy 600.

Fig. 23 shows the results of thermal analysis for two different points on the top surface at the middle of the plate (x=50 mm). Good agreement is observed between the thermal results of present study and those of Fanous et al. [].

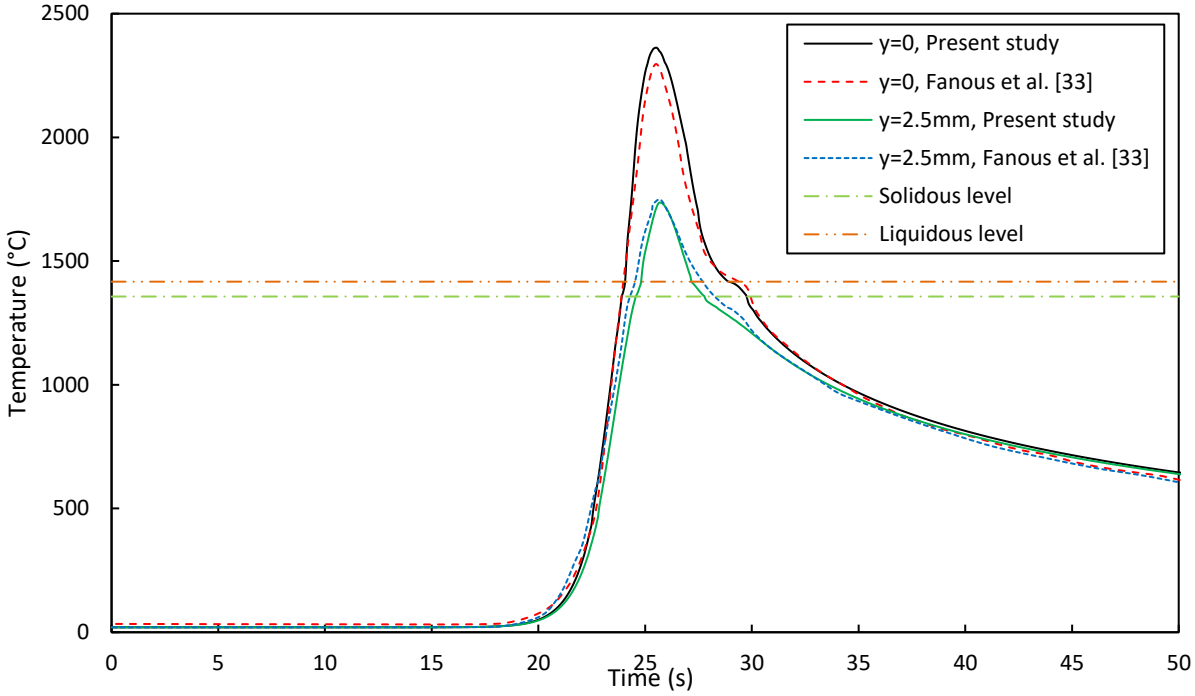

Fig. 23. Comparison of the results of temperature history for two different points on the top surface at the middle of the plate (x=50 mm)

6.1.5. Mechanical analysis

The thermal elasto-plastic material model, on the basis of the isotropic strain hardening rule and the von Mises yield criterion, was considered. Since the thermal elasto-plastic analysis is a non-linear problem, an incremental calculation technique was used to solve the problem.

The y component of the displacement of nodes located on the symmetry plane (Fig. 18) were set to zero due to loading and geometric symmetry. Also, during the heating step (welding process), the surfaces under clamping force in the experiment were fixed in the x, y and z directions, as shown in Fig. 18. In the next steps when the fixation of surfaces under the clamping force was released, displacement of one node on plane far from the weld line was constrained in the x and z directions and another node on the same plane was constrained in the z direction to keep structural stability.

After finishing the welding process, another step as shown in Fig. 17 was defined to create holes in the specimen using element death technique. Through this technique, the elements located at the position of the holes were deactivated using *MODEL CHANGE option in Abaqus.

6.1.6. Results of the mechanical analysis

Fig. 24 shows the results transverse component of stress (S_{22}) on the front surface at the end of each step. It should be mentioned that S_{22} is perpendicular to the crack plane and so it plays an important role during crack growth.

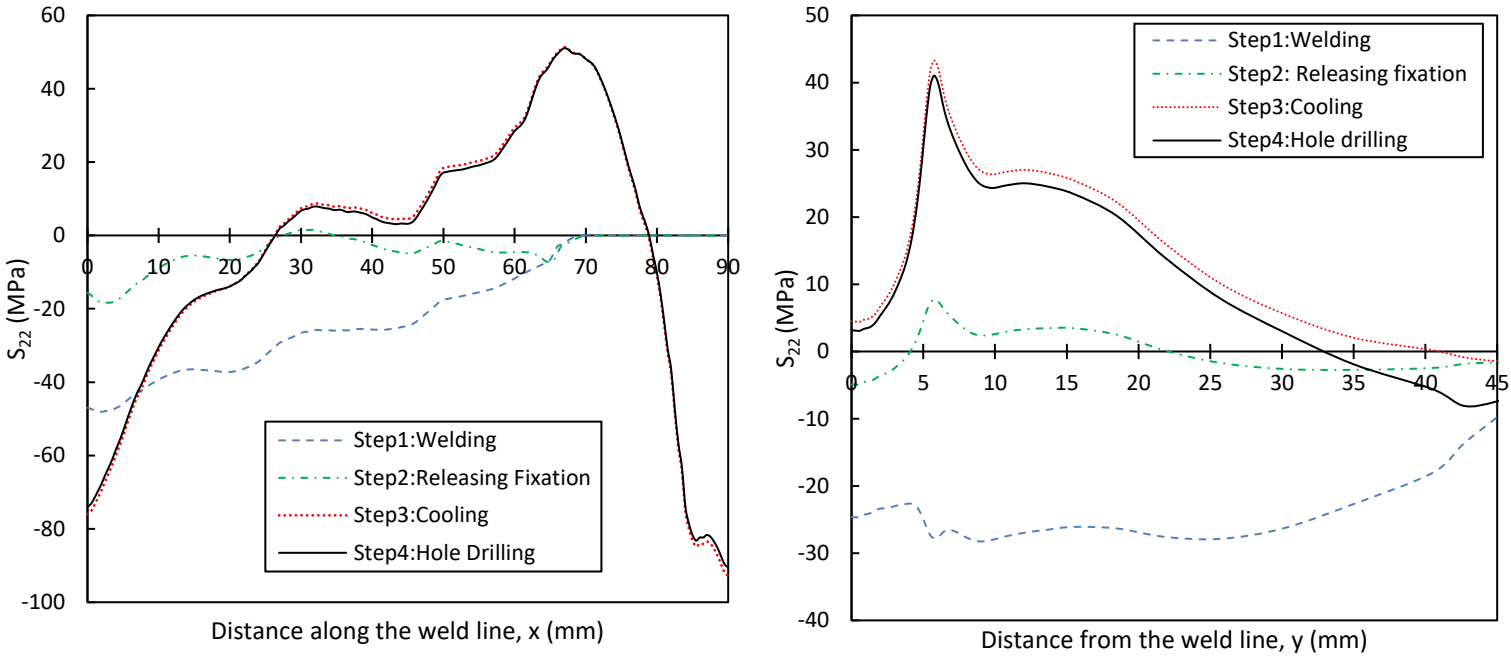

(a) (b)

Fig. 24. Distribution of longitudinal stress on the front surface (a) along the weld centerline, $y = 0$mm (b) perpendicular to the weld line at $x = 45$mm.

As can be seen from Fig. 24, during the welding process the stresses in regions with elevated temperature are noticeably low. By cooling down the specimen into the ambient temperature, the absolute amount of stresses increases and these stresses remain in the specimen as the residual stresses. The residual stresses in the specimen appear as a result of interaction of elastic strains with plastic strains accumulated during welding process. The residual stresses are self-balanced so, their values are tensile in some regions and compressive in others. In other words, the welding residual stresses satisfy the self-equilibrating condition between the tensile and compressive regions in a welded joint. It is seen that the amount of residual stresses in the specimens tested are considerable and they should be taken into account.

As can be observed from Fig. 24, by creating the holes in the specimen, distribution of residual stresses near the weld centerline remains almost constant. The amount of

stresses far from the weld line varies slightly since the portion of eliminated stresses should be tolerated by other regions.

The aforementioned procedure for calculating residual stresses was repeated for the specimen with flat geometry, i.e. the reinforcement geometry was neglected. The results of residual stresses for these tow geometries are compared in Fig. 25.

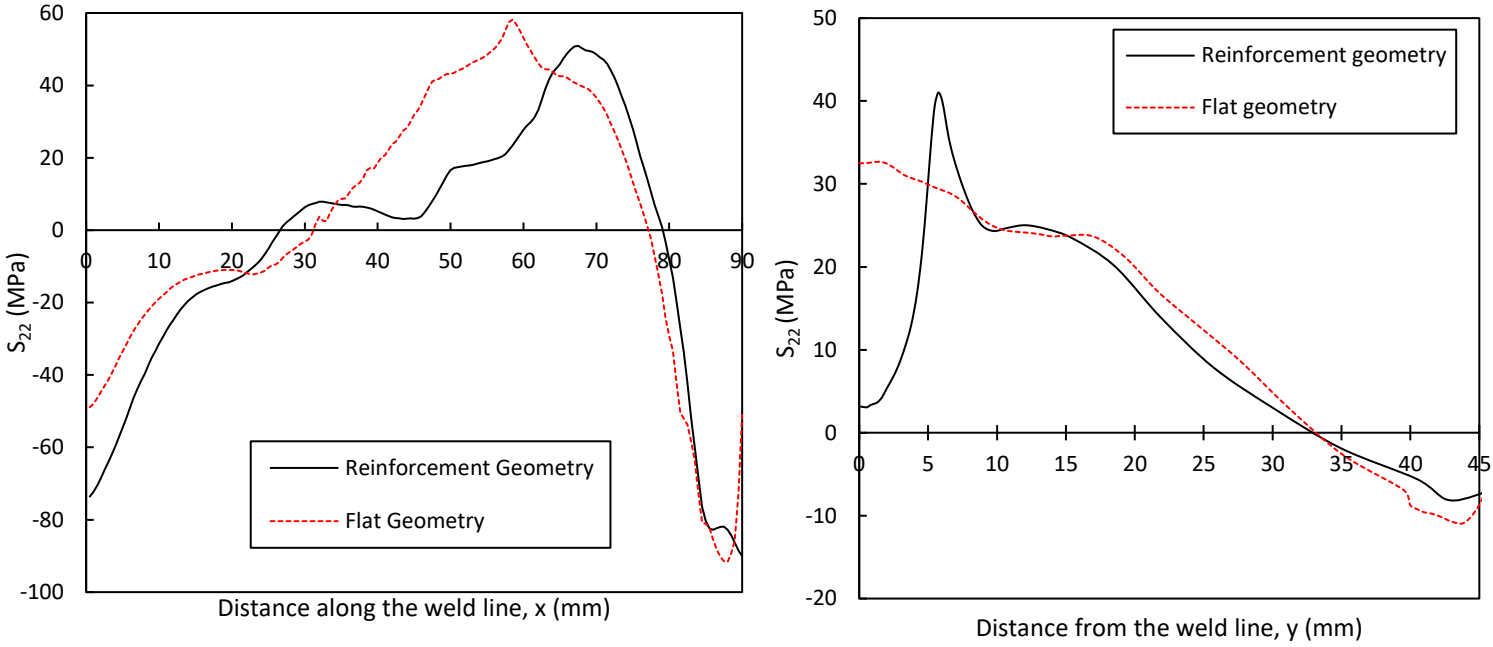

(a) (b)

Fig. 25. Comparison of the residual stresses in specimen with reinforcement geometry and flat geometry; (a) longitudinal stress on the front surface along the weld centerline, $y = 0$mm (b) transverse stress on the front surface at $x = 45$mm.

As can be seen from Fig. 25, by neglecting the geometry of the weld reinforcement in simulation, the distribution of residual stresses in the welded joint is changed.

Simulations of two other specimens (WM-HT and WM-Flat) were also conducted. For simulating WM-HT specimen, one thermal step and one corresponding mechanical step were added at the end of the thermal and mechanical analysis, respectively. In the thermal analysis, the variation of ambient temperature was set the same as that applied in the experiment. For this case, the convection coefficient was set to 20 $W/m^2\,°C$ due to the forced convection. In the mechanical analysis, the steady-state creep behavior was modelled by employing the hyperbolic-sine law as the following equation [35]:

$$\dot{\varepsilon}^{cr} = A[\sinh B\tilde{q}]^n \exp\left(-\frac{Q}{RT}\right) \quad (12)$$

where $\dot{\varepsilon}^{cr}$ is the uniaxial equivalent creep strain rate, $\tilde{q}$ is the uniaxial equivalent deviatoric stress (for isotropic creep, $\tilde{q}$ is Mises equivalent stress), Q is the activation energy, R is the universal gas constant ($8314\ \frac{\text{kJ}}{\text{mol.K}}$), T is the temperature and A, B and n are material constants. In case of Al5083-H111, Q, A, B and n are 152 kJ/mol, 6.7×10^{10} min^{-1}, 0.025 MPa^{-1} and 3, respectively [35].

For simulating WM-Flat specimen, at first, one step was added at the end of the mechanical analysis to simulate removing the weld reinforcements. In this step, the weld reinforcements were removed from both sides of the specimen using element deactivation. Then, the heat treatment was applied to the specimen as mentioned formerly. The results of residual stress redistribution for these two specimens are illustrated in Fig. 26.

It should be noted that post weld heat treatment and removing the weld reinforcements, may modify microstructure and there has been no attempt to include this in the present model.

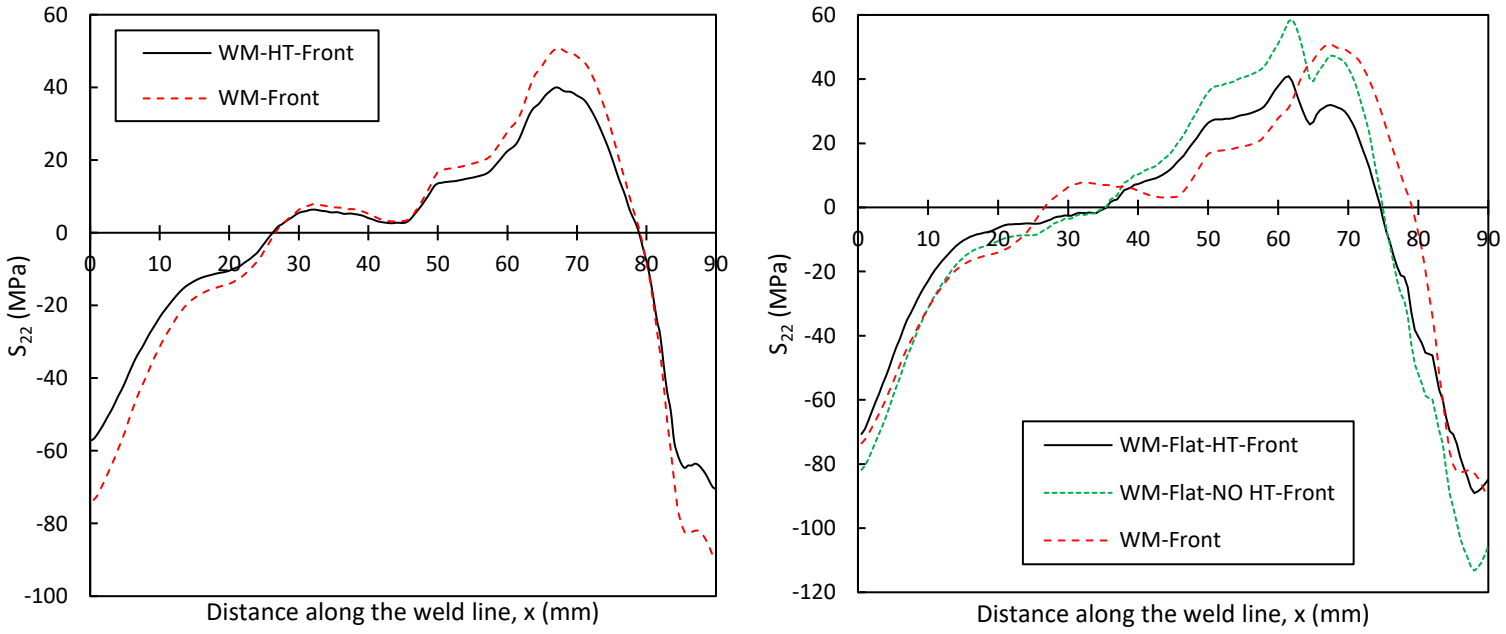

(a) (b)

Fig. 26. Distribution of transverse component of residual stress along the weld line for (a) WM-HT (b) WM-Flat.

As can be seen from Fig. 26a, due to the post weld heat treatment the magnitude of the residual stresses is decreased while, the shape of distribution of residual stresses is not changed. On the other hand, by removing the weld reinforcements, residual stresses are redistributed in such a way that the magnitude of maximum and minimum of residual stresses is increased (Fig. 26b). This occurs for the reason that the portion of eliminated stresses which existed in the removed regions, should be tolerated by remained material. Thereafter, by applying the post weld heat treatment to the specimen the magnitude of the residual stresses is decreased without change in form of residual stresses distribution.

6.2. Redistribution of residual stresses due to crack growth

Simulation of fatigue crack growth was conducted using Zencrack in order to obtain variation of SIF due to the redistribution of residual stresses caused by crack growth. Details of fatigue crack growth simulation was described in Section 4. Residual stresses obtained from welding simulation were imported to the analysis as predefined field. The total SIF can be obtained by adding those obtained from the external applied load and from the residual stresses. So, it can be expressed as:

$$K_{tot} = K_{applied} + K_{Res} \tag{13}$$

where $K_{applied}$ and K_{Res} are SIFs caused by external applied load and by residual stresses, respectively. Substituting $K_{applied}$ which was formerly obtained in Section 4, K_{Res} can be calculated from Eq. (13). The results of variation of K_{Res} caused by crack growth is illustrated in Fig. 27.

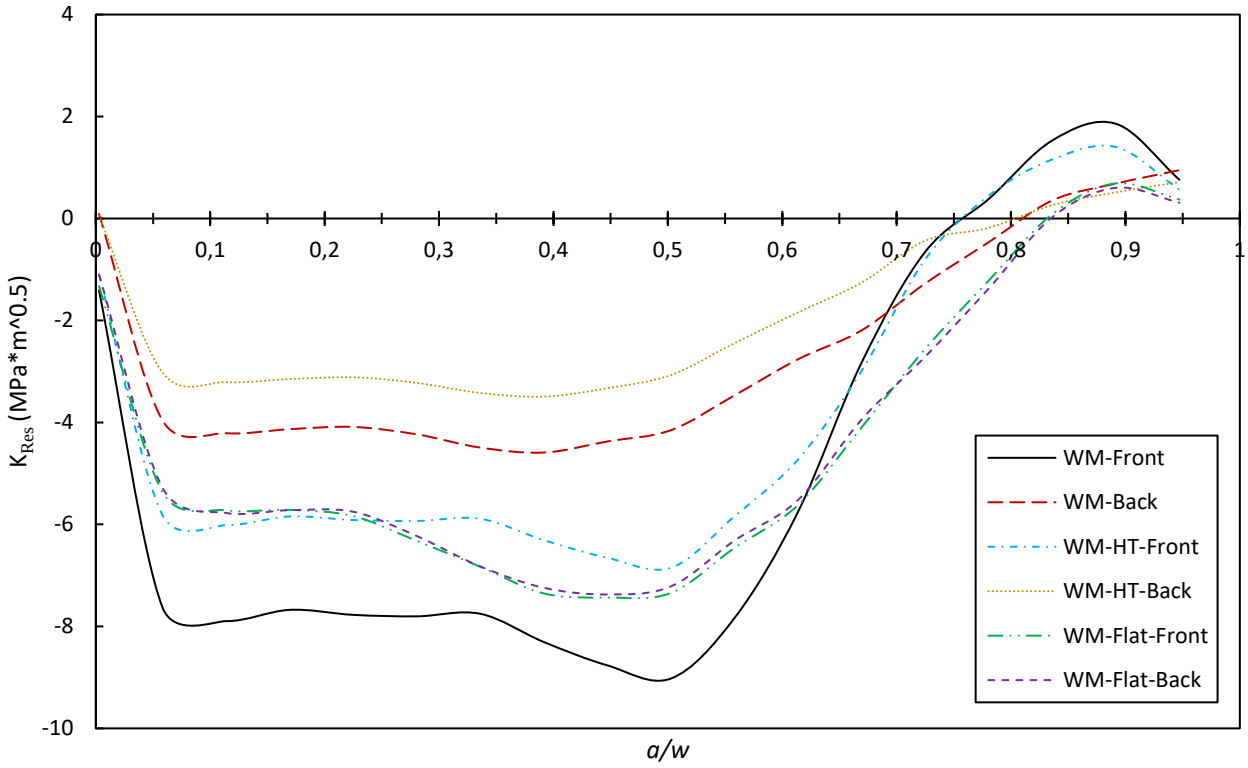

Fig. 27. Variation of K_{Res} during crack growth for various specimens.

As the crack grows the magnitude of SIF firstly increases and then it slightly changes. In all cases, after the dimensionless crack length exceeds $a/w > 0.5$, the magnitude of SIF gradually decreases due to releasing residual stresses and thereafter, in a short range, K_{Res} becomes positive.

In the present investigation, the transverse component of residual stress (S_{22}) is perpendicular to the crack plane and so K_{Res} is directly influenced by that. According to the Fig. 26, S_{22} is compressive at the edge of the weld centerline and subsequently as can be seen from Fig. 27, the SIF is negative when the crack is initiated from that area. By growing the crack, residual stress in the region around the crack is released and subsequently residual stress is redistributed in the ligament. As redistribution of transverse component of residual stress is schematically illustrated in Fig. 28, the crack front is located in the compressive stress field in the wide range.

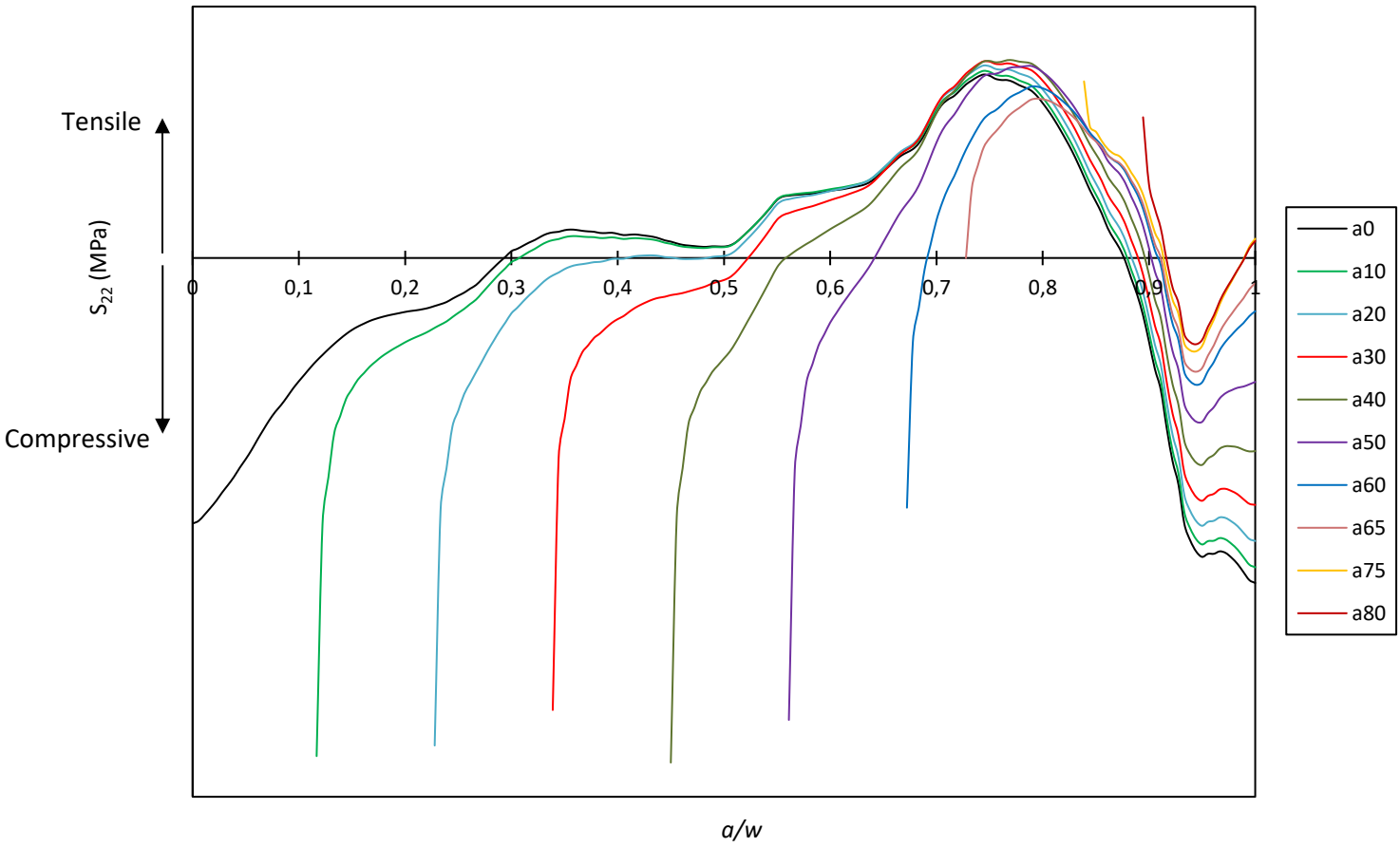

Fig. 28. Redistribution of transverse component of residual stress as crack grows at the front side of WM specimen.

Also, it can be seen from Fig. 27 that the compressive SIF on the front side of WM and WM-HT specimens is greater than the back side and accordingly, the fatigue crack growth rate on the front side is smaller than that on the back side for $\Delta K_{\mathrm{I,local}}$ values less than 15 MPa$\sqrt{\mathrm{m}}$ (Fig. 16). It can be seen from Fig. 16, as the crack grows, the crack closure is weakened and the fatigue crack growth rates of the front and back side of the specimen become the same due to releasing residual stresses.

Effective SIF range is defined as Eq. (14):

$$\Delta K_{eff} = \begin{cases} \Delta K_{tot} = \left(K_{applied,max} + K_{Res}\right) - \left(K_{applied,min} + K_{Res}\right) & K_{applied,min} + K_{Res} > 0 \\ K_{tot,max} = \left(K_{applied,max} + K_{Res}\right) & K_{applied,min} + K_{Res} \leq 0 \end{cases} \quad (14)$$

Fig. 29 shows fatigue crack growth rates in terms of ΔK_{eff} for all specimens.

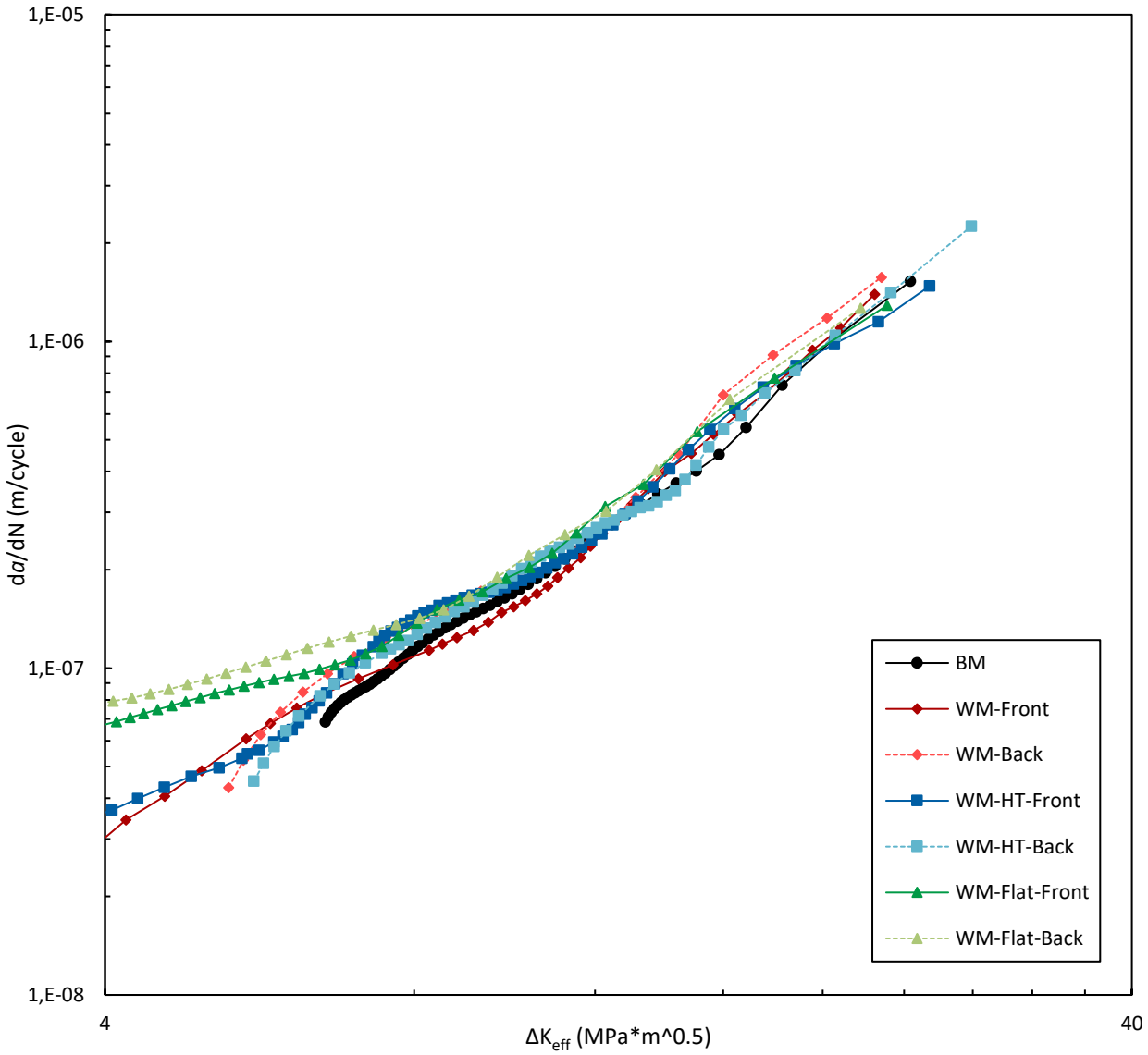

Fig. 29. Crack growth rate versus ΔK_{eff} for all specimens.

As can be seen from Fig. 29, FCGRs data for BM, WM and WM-HT specimens tend to fall within a very narrow scatter band when FCGRs are plotted in terms of ΔK_{eff} calculated from Eq. (14). Thus, redistribution of residual stresses allow the reduction of FCGRs data to a unique curve $da/dN - \Delta K_{eff}$ once the effect of residual stresses redistribution as well as real geometry of weld are accounted for.

FCGRs of WM-Flat specimen, for ΔK_{eff} values below 6.5 MPa$\sqrt{\text{m}}$, are higher than other specimens which implies that the calculated residual SIFs (K_{Res}) from simulation are higher than those existed in the specimen. This occurs due to the fact that some parts of the residual stresses were released during mechanical operation of removing the weld reinforcements.

7. Conclusions

In the present paper, the effect of redistribution of residual stresses as well as the weld reinforcements and post weld heat treatment on fatigue crack growth of Al5083-H111 have been investigated experimentally and numerically. According to the obtained results, the following conclusions can be drawn:

- It was shown that 27% error occurs in calculation of SIF by neglecting the geometry of the weld reinforcement.
- Fatigue crack grows asymmetrically in the welded zone due to the shape of weld reinforcements. The crack firstly initiates from front side of weldment and then, the shape of the crack front changes in such a manner that the crack grows under K_{I}-constant conditions.
- The experimental results showed that the FCGRs of the front and back sides of all specimens gradually become closer to each other and then they become equal. Simulating welding process it was shown that this is due to releasing residual stresses.
- It was numerically shown that by initiating the crack the magnitude of SIF firstly increases and then it varies slightly. After the crack length exceeds $a/w > 0.5$, the magnitude of SIF gradually decreases due to releasing residual stresses. Also, it was shown that geometry of the weld reinforcements and post weld heat treatment affects the distribution of residual stresses.
- Considering redistribution of residual stresses in the effective stress intensity factor range (ΔK_{eff}), the satisfactorily correlation was observed between the FCGRs data of welded joints with base metal.

References

[1] Wilcox DV, Adkins H, Dickerson PB, Hasemeyer EA, Lockwood L. Welding aluminum. 6th ed. American welding society, Florida, 1972.

[2] Mutombo K, Du Toit M. Mechanical properties of 5083 aluminium welds after manual and automatic pulsed gas metal arc welding using E5356 filler. Mat Sci Forum 2010;654-6:2260-3.

[3] Nguyen TN, Wahab MA. The effect of weld geometry and residual stresses on the fatigue of welded joints under combined loading. J Mater Process Technol 1998;77:201-8.

[4] McClung RC. A literature survey on the stability and significance of residual stresses during fatigue. Fatigue Fract Engng Mater Struct 2007;30:173-205.

[5] Ma YE, Irving P. Residual stress effects and fatigue behavior of Friction-Stir-Welded 2198-T8 Al-Li alloy joints. J Aircraft 2011;48(4):1238-44.

[6] Shahani AR, Shakeri I. Experimental evaluation of fatigue behavior of thin Al5456 welded joints. Fatigue Fract Engng Mater Struct (accepted) DOI: 10.1111/ffe.13173

[7] Shi YW, Chen BY, Zhang JX. Effects of welding residual stresses on fatigue crack growth behaviour in butt welds of a pipeline steel. Eng Fract Mech 1990;36(6):893-902.

[8] Ma S, Zhang XB, Recho N, Li J. The mixed-mode investigation of the fatigue crack in CTS metallic specimen. Int J Fatigue 2006;28:1780-90.

[9] Garcia C, Lotz T, Martinez M, Artemev A, Alderliesten R, Benedictus R. Fatigue crack growth in residual stress fields. Int J Fatigue 2016;87:326-38.

[10] Shahani AR, Farrahi A. Experimental investigation and numerical modeling of the fatigue crack growth in friction stir spot welding of lap-shear specimen. Int J Fatigue 2019;125:520-9.

[11] Lee YB, Chung CS, Park YK, Kim HK. Effects of redistributing residual stress on the fatigue behavior of SS330 weldment. Int J Fatigue 1998;20(8):565-73.

[12] Miyazaki K, Mochizuki M, Kanno S, Hayashi M, Shiratori M, Yu Q. Analysis of stress intensity factor due to surface crack propagation in residual stress fields caused by welding. JSME Int J Series A Solid Mech Mater Eng 2002;45:199-207.

[13] Shiue RK, Chang CT, Young MC, Tsay LW. The effect of residual thermal stresses on the fatigue crack growth of laser-surface-annealed AISI 304 stainless steel Part I: computer simulation. Mat Sci Eng A 2004;A364:101-8.

[14] Sutton MA, Reynolds AP, Ge YZ, Deng X. Limited weld residual stress measurements in fatigue crack propagation: Part II. FEM-based fatigue crack propagation with complete residual stress fields. Fatigue Fract Engng Mater Struct 2006;29:537-45.

[15] Liljedahl CDM, Tan ML, Zanellato O, Ganguly S, Fitzpatrick ME, Edwards L. Evolution of residual stresses with fatigue loading and subsequent crack growth in a welded aluminium alloy middle tension specimen. Eng Fract Mech 2008;75:3881-94.

[16] Liljedahl CDM, Zanellato O, Edwards L, Fitzpatrick ME. Evolution of residual stresses with fatigue crack growth in a variable polarity plasma arc-welded aluminum alloy compact tension specimen. Metall Mater Trans A 2008;39(10):2370-7.

[17] Liljedahl CDM, Zanellato O, Lin J, Fitzpatrick ME, Edwards L. The effect of weld residual stresses and their re-distribution with crack growth during fatigue under constant amplitude loading. Int J Fatigue 2010;32:735-43.

[18] Servetti G, Zhang X. Predicting fatigue crack growth rate in a welded butt joint: The role of effective R ratio in accounting for residual stress effect. Eng Fract Mech 2009;76:1589-602.

[19] Shankar K, Wu W. Effect of welding and weld repair on crack propagation behaviour in aluminium alloy 5083 plates. Mater Des 2002;23:201-8.

[20] Zhu L, Jia MP. A new approach for the influence of residual stress on fatigue crack propagation. Results Phys 2017;7:2204-12.

[21] Hobbacher AF. Recommendations for fatigue design of welded joints and components. 2nd ed. IIW Collection. Springer; 2016.

[22] Shen W, Yan R, Liu E, Xu L. Fatigue growth behavior for surface crack in welding joints under combined compressive and bending stresses. Int J Fatigue 2015;77:50-63.

[23] Richard H. A., Benitz K., “A loading device for the creation of mixed mode in fracture mechanics”, International Journal of Fracture, Vol. 22, Issue 2, pp. R55-R58, 1983.

[24] ASM handbook volume 9. Metallography and microstructures. ASM International; 1990

[25] Dassault Systèmes. Abaqus product documentation: Abaqus analysis user's manual, Version 6.14-2. Providence, RI, USA: Dassault Systèmes; 2014.

[26] Zentech International Limited. Zencrack user manual, Version 7.9-3. London, UK: Zentech International Limited, 2015.

[27] Richard HA. Fracture mechanical predictions for cracks with superimposed normal and shear loading. VDI-Forschungsheft 631/85. Düsseldorf: VDI-Verlag, 1985 (in German).

[28] Shahani AR, Shakeri I, Rans CD. Two engineering models for predicting the retardation of fatigue crack growth caused by mixed mode overload. Int J Fatigue (accepted). DOI: 10.1016/j.ijfatigue.2019.105378.

[29] ASTM E647-15e1. Standard test method for measurement of fatigue crack growth rates. West Conshohocken, PA: ASTM International; 2015.

[30] Summers, P.T., Chen, Y., Rippe, C.M. et al. Overview of aluminum alloy mechanical properties during and after fires. Fire Sci Rev 2015;4:3.

[31] Moein H, Sattari-Far I. Different finite element techniques to predict welding residual stresses in aluminum alloy plates. J Mech Sci Technol 2014;28(2):679-89.

[32] Friedman E. Thermomechanical analysis of the welding process using the finite element method. ASME J Pressure Vessel Technol 1975;97(3):206-13.

[33] Fanous IFZ, Younan MYA, Wifi AS. 3-D finite element modeling of the welding process using element birth and element movement techniques. ASME J Pressure Vessel Technol 2003;125(2):144-50.

[34] Dehkordi YG, Anaraki AP, Shahani AR. Study of the effective parameters on welding residual stress relaxation in aluminum cylindrical shells under cyclic pressure. Thin Walled Struct 2019;143. DOI: 10.1016/j.tws.2019.106235

[35] Maljaars J, Soetens F, Katgerman L. Constitutive model for aluminum alloys exposed to fire conditions. Metall Mater Trans A 2008;39:778-89.